

**A revised oxygen barometry in sulfide-saturated magmas and application to the Permian magmatic Ni–Cu deposits in the southern Central Asian Orogenic Belt**

Ya–Jing Mao<sup>a,b\*</sup>, Ke–Zhang Qin<sup>a,d</sup>, Stephen J. Barnes<sup>b</sup>, Clément Ferraina<sup>c</sup>, Giada Iacono–Marziano<sup>c</sup>, Michael Verrall<sup>b</sup>, Dongmei Tang<sup>a</sup>, Shengchao Xue<sup>c</sup>

<sup>a</sup> Key Laboratory of Mineral Resources, Institute of Geology and Geophysics, Chinese Academy of Sciences, Beijing 100029, China

<sup>b</sup> CSIRO Mineral Resources, Perth, 6151, Australia

<sup>c</sup> ISTO, UMR 7327 CNRS-Université d'Orléans–BRGM, 1A rue de la Ferrollerie, 45071 Orléans Cedex 2, France

<sup>d</sup> University of Chinese Academy of Sciences, Beijing 100049, China

<sup>e</sup> State Key Laboratory of Geological Processes and Mineral Resources, China University of Geosciences, Beijing 100083, China

***Mineralium Deposita***

\*corresponding author: Ya–Jing Mao, maoyajing@mail.iggcas.ac.cn

## 22    **Abstract**

23        Oxygen fugacity is a key parameter in controlling the petrogenesis of the mafic-  
24    ultramafic rocks and their associated sulfide mineralization, especially in convergent  
25    settings. This study uses new and previously published experimental data on olivine-  
26    sulfide pairs to reparametrize an expression for oxygen barometry using the distribution  
27    coefficient  $K_D^{\text{FeNi}}$  for Fe-Ni exchange between olivine and sulfide. We derive a new  
28    expression,  $\Delta\text{QFM} = (9.775 + 0.416 \cdot C_{\text{Ni}} - K_D^{\text{FeNi}}) / 4.308$ , where  $\Delta\text{QFM}$  denotes  
29    divergence from the fayalite–magnetite–quartz buffer. The revised oxygen barometry  
30    has been applied to the Permian magmatic Ni–Cu deposits in the Central Asian  
31    Orogenic Belt, NW China. The Ni–Cu deposits in the East Tianshan-North Tianshan,  
32    Central Tianshan, and Beishan-are considered as a single mineral system, whereas the  
33    spatially separated deposits in the East Junggar are considered as a separate system.  
34    The deposits of the East Tianshan group exhibits a large range of oxygen fugacity  
35    (QFM–2 to ~QFM +1) and Ni tenor (metal concentration in pure sulfide, ~5 wt.% to  
36    16 wt.%). The Poyi and Huangshannan deposits in east Tianshan contain high Ni tenor  
37    sulfides, varying from 12 to 16 wt.%. The relatively high Fo values (>85 mol.%) and  
38    Ni contents (>2000 ppm) in olivine of these deposits indicate that the high Ni tenor  
39    sulfides were segregated from less differentiated high-Ni magmas that also had  
40    relatively high oxygen fugacity (~QFM +1). The remaining Ni–Cu deposits in east  
41    Tianshan - the Huangshandong, Huangshanxi, Hulu, Tulaergen, Tudun, and  
42    Xiangshanzhong deposits - have intermediate Ni tenors (5–8 wt.%). These sulfides

correspond to the intermediate Fo values (80–84 mol.%) and Ni contents (700–1400 ppm) in the coexisting olivine, illustrating that they were segregated from magmas with lower Ni contents thought to be the result of a large amount (15–20%) of olivine fractionation at depth. These magmas are more reduced ( $-2 < \Delta\text{QFM} < +0.3$ ) than the less evolved magmas ( $\sim\text{QFM} + 1$ ). It is shown that  $\Delta\text{QFM}$  value calculated for the deposits in east Tianshan decreases with the decreasing Fo value, indicating that the host magmas became gradually reduced during evolution, which can be explained by primarily oxidizing magma progressively assimilating crustal material containing reducing agents, such as graphite. The Kalatongke deposit in the East Junggar belt, containing the lowest Ni tenors in sulfides (3–5 wt.%) and low Fo values in olivine ( $< 78$  mol.%), was derived from relatively oxidizing magmas ( $\sim\text{QFM} + 1$ ) that probably have experienced significant olivine plus clinopyroxene and plagioclase fractionation at depth. We propose that the variation in oxygen fugacity and Ni tenor in the Permian Ni–Cu deposits in the CAOBS is the result of gradual contamination and a variable degree of fractional crystallization.

**Key words:** Magmatic sulfide deposit, Oxygen barometer, Sulfide-olivine Fe-Ni exchange, Nickel tenor, Central Asian Orogenic Belt

## Introduction

Sulfur speciation in magma is controlled by its oxidation conditions. Strongly

oxidized magma will dissolve S as sulfate rather than sulfide (Jugo et al., 2009), giving rise to much higher S contents at sulfate rather than sulfide saturation. This variable may be critical in forming Ni–Cu deposits in convergent settings due to the relatively oxidized character of partial melts derived from supra-subduction zone mantle (Frost and McCammon 2008). Numerous experimental studies of iron and nickel partitioning between olivine and sulfide liquid under magmatic conditions (Brenan 2003; Brenan and Caciagli 2000; Fleet and MacRae 1988; Gaetani and Grove 1997) demonstrate that the oxygen fugacity ( $fO_2$ ), or more precisely the ratio of ferric to ferrous iron in the magma for which  $fO_2$  is a proxy, plays a role in determining compositions of olivine and coexisting sulfide liquid. The Fe–Ni equilibrium between sulfide and coexisting olivine is often expressed as an exchange coefficient ( $K_D$ ):

$$K_D = (X_{NiS}/X_{FeS})_{\text{sulfide liquid}} / (X_{NiO}/X_{FeO})_{\text{olivine}} \quad (1)$$

where  $X_i$  is equal to the mole fraction of component  $i$  in the phase of interest. Brenan and Caciagli (2000) found that  $K_D$  is a function of both  $fO_2$  and sulfide melt Ni content and that the variation in  $K_D$  recorded by natural samples can be reconciled in terms of changes in both these parameters at the magmatic stage.  $K_D$  can be estimated using the compositions of olivine and the coexisting magmatic sulfide assemblage in natural systems and be used as an indicator of their oxidation state (Barnes et al. 2013; Brenan and Caciagli 2000). However, experimental data that have yielded at relatively oxidizing and low Ni tenor in sulfide are rare.

The magmatic Ni–Cu deposits in the Central Asian Orogenic Belt (CAOB), NW

85 China, were emplaced within an orogenic belt at the post-subduction stage (Li et al.  
86 2012; Qin et al. 2011; Song et al. 2013; Su et al. 2011), in contrast to the more typical  
87 intra-plate craton margin setting of Ni–Cu dominant magmatic sulfide deposits (Maier  
88 and Groves 2011). Deposits in convergent-margin orogenic belts have received  
89 increasing attention after the discovery of some substantial Ni–Cu deposits in such  
90 settings, such as the Nova Ni–Cu deposit in Albany–Fraser belt in western Australia  
91 (Maier et al. 2016) and the Xiarihamu Ni–Cu deposit in Tibet plateau in west China (Li  
92 et al. 2015). The cluster of Ni–Cu deposits in NW China offer a great opportunity to  
93 study the oxygen fugacity and its controlling factor of the Ni–Cu deposits in such  
94 tectonic setting. Zircon U–Pb studies reveal that the majority of these intrusions in NW  
95 China were emplaced during the Permian (Qin et al. 2011; Su et al. 2011). These  
96 Permian Ni–Cu deposits contain ~300 Mt reserves at average grades of 0.5 wt.% Ni  
97 and 0.3 wt. % Cu, representing one of the most important Ni provinces in China (Mao  
98 et al. 2008). Although these deposits occur in different tectonic terranes, representing  
99 different accretionary arcs or micro–continents (Jahn 2004; Xiao et al. 2009), they have  
100 several similarities in terms of emplacement age, geochemical features, and thus source  
101 characteristics (Deng et al. 2014; Gao and Zhou 2013; Han et al. 2004; Li et al. 2012;  
102 Mao et al. 2014a; Mao et al. 2016; Qin et al. 2011; Song and Li 2009; Su et al. 2011;  
103 Sun et al. 2013b; Tang et al. 2011; Tang et al. 2013; Xue et al. 2016; Zhang et al. 2009;  
104 Zhou et al. 2004). Nevertheless, there are also several differences among these deposits,  
105 such as host rocks, sulfide textures, Ni and platinum group elements (PGEs) tenors in

sulfides, and olivine compositions (Mao et al. 2017; Qin et al. 2012; Su et al. 2013). The close spatial and tectonic association of these deposits makes them a good case study for a series of deposits forming part of a single mineral system, having a probable derivation from a common mantle source, but undergoing different paths towards emplacement.

In this study, a revised equation is presented for the  $fO_2$  dependence of the olivine/sulfide Fe/Ni  $K_D$  based on a revised calibration using some new experimental data. The Permian Ni–Cu deposits in east Tianshan are considered as components of a single mineral system. The revised equation is applied to the Permian deposits, using the technique of microbeam XRF mapping to estimate the Ni tenor of the sulfide component of these deposits. Integrating these data with the coexisting olivine composition, we estimate the oxygen fugacity and Ni tenor variations of these deposits and their controlling factors. The major aim of the contribution is to understand the processes that control the variability of oxygen fugacity and Ni tenor of the magmatic Ni–Cu systems in orogenic belts, using a series of comagmatic deposits forming part of a single mineral system.

## **Overview of the Permian magmatic Ni–Cu deposits in NW China**

Economic Ni–Cu deposits discovered to date in the CAOB are restricted to the southern margin, including the Hongqiling No.7 deposit in NE China and the cluster of Ni–Cu deposits in NW China (Fig. 1). The most important discovery of Ni–Cu deposits in NW China, the Huangshandong and Huangshanxi deposits in the North Tianshan and

the Kalatongke deposit in the East Junggar (Table 1), was made in the 1980s (Wang and Zhao 1991; Wang et al. 1987). Subsequently, a number of other mafic-ultramafic intrusions were found to host magmatic sulfides, such as the Xiangshan, Huangshanxi, Tudun, and Hulu deposits (Table 1). In the 2000s, some additional discoveries were made such as the Tulaergen deposit in the east part of North Tianshan (San et al. 2003) and the Baixintan occurrence in the west part of North Tianshan (Li et al. 2014) (Fig. 2). In addition, economic Ni–Cu ore bodies had been outlined in the Poyi and Poshi mafic–ultramafic intrusions in the Beishan Terrane (Xia et al. 2013). The Permian emplacement age of the Huangshandong, Huangshanxi, and Kalatongke deposits was first established by Han et al. (2004) and Zhou et al. (2004) using zircon U–Pb dating. The main features of some of these deposits have been reviewed by Mao et al. (2008) and Lightfoot and Evans–Lamswood (2015). Between 2008 and 2016, numerous case studies, including precise dating, whole rock geochemical analysis and studies of mineral composition and PGE concentrations have been carried out on these Ni–Cu deposits (Zhang et al. 2009, 2011; Tang et al. 2011; Sun et al. 2013a; Deng et al. 2014; Mao et al. 2014a, 2015; Yang et al. 2014; Zhao et al. 2015; Xue et al. 2016).

The Ni–Cu deposits in NW China mainly occur in four terranes, the Beishan, Central Tianshan, North Tianshan and East Junggar from south to north (Fig. 2). The Beishan, Central Tianshan, and North Tianshan terranes are named as east Tianshan in this study. The Beishan Terrane is located in the northeastern part of the Tarim craton, adjacent to the Central Tianshan Terrane in the north (Fig. 2). It is mainly composed of

148 the Precambrian crystalline basement and overlying sedimentary rocks, namely  
149 Archean granitic gneiss, Paleoproterozoic amphibolite, gneiss, schist, quartzite, and  
150 marble, overlain by Carboniferous volcanic and sedimentary rocks (BGMRXUAR  
151 1993). Magmatic sulfide-bearing mafic-ultramafic intrusions, such as the Poyi and  
152 Poshu Ni-Cu deposits, the Bijiaoshan, Xuanwoling, and Hongshishan occurrences, are  
153 widespread in the Beishan Terrane. Most of those intrusions are characterized by minor  
154 Ni-Cu mineralization with low Ni grade and high proportions of olivine (Su et al. 2013;  
155 Xia et al. 2013; Xue et al. 2016). Olivines in these intrusions tend to have high forsterite  
156 (Fo) values and high Ni contents, significantly higher than those in neighboring terranes.  
157 The Central Tianshan Terrane is composed of the Precambrian crystalline basement  
158 including the Mesoproterozoic Xingxingxia Group and Kawabulak Group. These  
159 Groups are dominated by gneisses, schists, marbles, and phyllites (BGMRXUAR,  
160 1993). The Tianyu and Baishiquan are two mineralized intrusions in the Central  
161 Tianshan (Chai et al. 2008; Tang et al. 2011). The North Tianshan Terrane is dominated  
162 by well-developed Devonian-Carboniferous strata, granites, and mafic-ultramafic  
163 complexes (BGMRXUAR, 1993). The lower Devonian to lower Carboniferous rocks  
164 mainly comprise sandstone, pelitic slate, siltstone, mudstone, pyrite-bearing mudstone,  
165 and limestone. The middle to upper Carboniferous strata is composed of mafic to  
166 intermediate volcanic rocks with abundant chert and limestone. The Baixintan Ni-Cu  
167 occurrence is located in the west part of the North Tianshan. A number of economic Ni-  
168 Cu deposits, e.g. the Huangshandong, Huangshanxi, Huangshannan, Xiangshanzhong,



and Tudun deposits occur in the central part (Huangshan camp), whereas the Tulaergen and Hulu deposits occur in the east part (Fig. 2). The Xiangshanzhong deposit represents the central part of the Xiangshan complex, which has been divided into three parts from west to east: the Xiangshanxi Ti–Fe mineralized segment, Xiangshanzhong Ni–Cu related segment, and Xiangshandong currently sulfide barren segment. The East Junggar orogenic belt comprises several metasedimentary and ophiolite assemblages, dominated by the Devonian rocks consisting of calc–alkaline volcanics and marine clastic sediments overlain by thick Carboniferous marine clastic sedimentary successions (BGMRXUAR 1993). The Kalatongke mafic intrusion is the only economic Ni–Cu deposit in the East Junggar (Fig. 2), but a few small Permian mafic–ultramafic intrusions with Ni–Cu mineralization close to the Kalatongke intrusion have been discovered in the 2010s, e.g. the Kemozibayi intrusion.

The common features of the Permian Ni–Cu deposits are as follow: (1) Small intrusions in size with surface area less than 3 km<sup>2</sup>, showing a spectrum of morphologies including rhomboid–shaped funnels, dyke–sill transitions and oblate channels (Barnes et al. 2016; Lightfoot and Evans-Lamswood 2015; Qin et al. 2012); (2) The intrusions are within strike–slip transtensional zones and are located at jogs or cross–linking structures, forming in open systems by multiple magma pulses (Lightfoot and Evans-Lamswood 2015; Mao et al. 2014b); (3) intrusions from the different tectonic terranes were emplaced within a narrow range of ages, from 270 to 290 Ma (Qin et al. 2011), coeval with the flood basalt in the Tarim craton (Tian et al. 2010); (4) The occurrence

of hydrous minerals, such as hornblende, phlogopite, and biotite in some intrusions, together with the arc-like geochemical character, suggesting the parental magmas were derived from a mantle source previously metasomatized by slab-derived fluids (Mao et al. 2015; Su et al. 2011); (5) crustal contamination, probably crustal sulfide contamination, is the key factor in triggering sulfide saturation (Mao et al. 2016; Xue et al. 2016); (6) the sulfide assemblage is dominated by pentlandite, pyrrhotite, and chalcopyrite, and PGE contents in these sulfides are low (Mao et al. 2017; Tang et al. 2011; Xue et al. 2016; Yang et al. 2014).

Apart from the Kalatongke deposit, which has relatively high Ni and Cu grades (0.6–0.9 wt.% for Ni and 1.1–1.4 wt.% for Cu ), the other Ni–Cu deposits in NW China are of low Ni and Cu grades (Table 1). The Ni–Cu mineralization of these deposits occurs in both ultramafic rocks (dunite, lherzolite, olivine websterite) and mafic rocks (olivine gabbro, gabbro). The deposits related to mafic rocks tend to have higher sulfur abundances than those related to ultramafic rocks. For mineralization associated with ultramafic rocks, such as the Huangshandong (ultramafic unit), Huangshanxi, Huangshannan, and Poyi intrusions, the sulfide textures are dominated by disseminated texture (sulfide content less than 20 wt.%), with minor net-textured and massive textures (less than 20%, Fig. 3). In contrast, mineralization associated with the mafic rocks, e.g. the Huangshandong mafic unit and Kalatongke deposits, has a wide range of sulfide textures. Net-textured and massive textures are the dominant ores in these deposits, whereas the disseminated ore accounts for less than

211 30 % (Fig. 3).

212

## 213 **Experimental and analytical procedures**

### 214 *Experimental and analytical methods of Fe-Ni exchange between olivine and sulfide*

215 A picritic gabbro-dolerite (from Noril'sk 1 intrusion ) was used as starting material  
216 for our experiment. The rock was powdered and melted at 1600 °C and atmospheric  
217 pressure for 2 hours into a homogenous volatile-free glass. Experiments were  
218 conducted in internally heated pressure vessels equipped with a rapid quench device at  
219  $1200 \pm 2$  °C,  $66 \pm 2$  MPa during 1 to 3 hours at the CNRS-ISTO, France (Table 2). The  
220 powdered starting glass was loaded into Pt capsules (internal diameter 5.7 mm) with  
221 the addition of 2 wt.% H<sub>2</sub>O and 5 wt.% S. The  $fO_2$  varied between  $-0.78$  and  $2.11$  log  
222 units relative to the QFM buffer, by adapting the partial pressure of hydrogen in the  
223 vessel. The redox solid sensor method (Co-Pd-CoO; Taylor et al., 1992) was also  
224 employed to check the  $fO_2$ : two pellets of CoPd metal mixtures and CoO were placed  
225 in a Pt capsule in the presence of excess H<sub>2</sub>O, and run at the same time of the samples,  
226 but for a longer duration (3-4 days, in order to reach the equilibrium). The  $fO_2$  of the  
227 sensor is determined by the composition of its metallic phases, following Taylor et al.  
228 (1992), and the  $fO_2$  of each charge then calculated following Botcharnikov et al. (2008)  
229 considering the activity of H<sub>2</sub>O estimated for every charge. Calculated  $fO_2$  are presented  
230 in Table 2. Every capsule was verified to have remained sealed during the experiments

by checking its weight after the experiment. The capsules were then cut half along their long axis, mounted in epoxy resin and polished for further analysis.

Olivine crystals and sulfide globules in each experimental sample were recognized by scanning electron microscopy (ZEISS Merlin compact FEG-SEM at CNRS-ISTO, France), and analyzed for their major element composition and Ni contents by electron microprobe (Cameca SX Five at CNRS-ISTO, France). Operating conditions for both sulfide and olivine were 20 kV accelerating voltage, 30 nA beam current, 10 s peak counting time for each element, except Ni for olivine (120 s), and O for sulfides (120 s). A focused beam was used for olivine, whereas the size of the spot was adapted to that of the sulfide droplet. Standards deviations for major elements in olivines and Fe, S concentrations in sulfide are less than 5 %. For Ni in sulfides, standard deviations are less than 20 % in samples containing more than 1 wt.% Ni in sulfide. Nickel content in olivine shows a more important variation (between 30 and 70 %) due to the low values close to the detection limit (i.e.  $\sim 100$  ppm). Sulfur fugacity ( $f_{S_2}$ ) was calculated from the experimental temperature, pressure,  $f_{O_2}$  and total FeO content of the silicate melt, using the equation in Mungall and Brenan (2014).

#### *Analysis of olivine and pentlandite compositions of natural samples*

Olivine analyses in this study were obtained from polished thin sections of the mineralized samples. The composition of olivine from the Xiangshanzhong deposit was obtained by wavelength-dispersive microprobe analysis using a JEOL JXA8100

electron probe at the Institute of Geology and Geophysics, Chinese Academy of Sciences. The operating conditions were 15 kV accelerating voltage, 12 nA beam current, 5  $\mu$ m beam size and 30 s peak counting time. Nickel and Ca in olivine were analyzed using a beam current of 20 nA and a peak counting time of 100 s. The detection limit for Ni and Ca under such conditions is ~200 ppm. The composition of olivine from the Kalatongke and Tudun deposits were analyzed at the Centre for Microscopy, Characterization and Analysis, The University of Western Australia, using a JEOL JXA8530F electron microprobe equipped with five tunable wavelength dispersive spectrometers. Operating conditions were 40 degrees take-off angle, a beam energy of 20 keV, a beam current of 150 nA and a peak counting time of 100 s. The detection limit for Ni and Ca under such conditions is ~50 ppm.

Nickel, Fe, Co, and S contents in pentlandite were determined by scanning electron microscope-based energy dispersive spectrometry (SEM-EDS), at CSIRO, Perth. SEM-EDS analyses were performed on carbon-coated, polished thin sections using a Zeiss Ultra-Plus field emission gun (FEG) SEM coupled with a Bruker X-Flash energy dispersive X-ray (EDX) detector for elemental analyses. An accelerating voltage of 20 kV and a beam current of 3 nA were used. The analysis time per analyses was set as 120 seconds. The coefficient of variations of Fe, S, and Ni contents in pentlandite yielded from repeated analysis on the same pentlandite grain are less than 1.1%, whereas the coefficient of variation of Co content in pentlandite is less than 4.5 %.

271 *Calculation of sulfide composition using XRF images*

272       The images of sulfide bearing samples used for 100% sulfide composition  
273 calculations were obtained using the desktop X-ray fluorescence M4 Tornado™  
274 instrument at CSIRO, Perth, equipped with a rhodium target X-ray tube operating at  
275 50 kV and 500 nA without filters and an XFlash® silicon drift X-ray detector. Maps  
276 were created using a 40 µm spot size on a 40 µm raster with dwell times of 10 ms per  
277 pixel. Maps are represented as un-quantified background-corrected peak height data  
278 for Kα peaks for each element, scaled linearly between minimum and maximum  
279 measured counts over the sample. Image processing software, ImageJ (version 1.50i),  
280 was used to analyze the modal proportions of sulfide minerals, based on the S, Cu, Ni  
281 single elemental distribution (S, Cu, and Ni representing the proportion of pyrrhotite,  
282 chalcopyrite, and pentlandite, respectively). The weight percentages of pentlandite,  
283 chalcopyrite, and pyrrhotite in sulfides were calculated based on the volume  
284 proportions of the sulfide minerals, assuming the density of pentlandite, chalcopyrite,  
285 and pyrrhotite as 4.8 g/cm<sup>3</sup>, 4.2 g/cm<sup>3</sup>, and 4.7 g/cm<sup>3</sup>, respectively. These results,  
286 together with pentlandite and pyrrhotite compositions yielded from SEM-EDS, were  
287 used to estimate the weight percentages of Ni, Cu, and Fe in the 100% sulfide  
288 composition. In the calculation, we used a uniform pyrrhotite composition of Fe<sub>0.9</sub>S for  
289 all of the deposits according to SEM-EDS analysis, and assumed the Cu is distributed  
290 in standard formula chalcopyrite. The sulfide assemblage has been observed to be  
291 chalcopyrite, pyrrhotite, and pentlandite in all the deposits.

Before analyzing the proportion of pentlandite and chalcopyrite, two steps are necessary to precisely estimate the sulfide composition using XRF images. Firstly, applying a threshold to Cu and Ni images to decrease the X-ray signal derived from beneath the sample surface and/or the background, which may cause overestimate of the Ni and Cu tenors. Although most of the Ni and Cu are consistently distributed within S, some Ni and Cu occur outside of the sulfur region (Fig. 4), probably resulting from Ni and Cu signal from sulfide beneath the sample surface. Thus, we created an inverse of the S image, a “non-S”, which was then subtracted to the Cu and Ni images, yielding modified Cu and Ni images. This step restricts the Cu and Ni signals to those originated from the sample surface, consistent with the S signal that derives from the surface. Subsequently, S image was combined with modified Cu and Ni images and the areas of these three elements represent the 2D volume proportions of chalcopyrite, pentlandite, and pyrrhotite.

The calculated Ni tenors of the Tudun and Huangshanxi deposits using this method, at both hand-sample and thin-section scales (Fig. 5), are consistent with the Ni contents calculated for 100% sulfide from measured S, Cu, and Ni concentrations in whole rock (Mao et al. 2014a). The error of Ni tenor calculated using these two methods are within 1 wt.% for most of the samples (Fig. 5a). For sulfides from NW China, the results of Ni tenor calculated by XRF images at thin section scales are comparable to those estimated by whole rock data of hand sample size. On the other hand, Cu contents in sulfides calculated by XRF images at thin-section scale tend to be more scattered than

these estimated at hand-sample scale as well as these by whole rock compositions (Fig. 5b). This may be due to the mobility of Cu at both late magmatic and hydrothermal stages. However, the calculated Cu contents in sulfides at thin section scale are within 2 wt.%. In addition, the samples chosen for the comparison have sulfur contents varying from 0.87 wt.% to 4.6 wt.%, representing low-grade ores. The Ni tenors in sulfides yielded from XRF images (Fig. 4) agree with those calculated by whole rock S, Ni, Cu data (Fig. 5). The advantage of sulfide composition estimation using the XRF image compared to the traditional calculation based on the whole rock composition is primarily that it removes the large uncertainty in the silicate Ni background for sulfide samples ( $S < 2$  wt.%), which is the primary source of uncertainty in the calculated metal tenors (Barnes et al. 2011).

## Results

### *Experimental results of Fe-Ni exchange between olivine and sulfide*

The experimental products consisted of glass, olivine crystals, sulfide globules (Fig. 6), and minor gas bubble (Fig. 6b). The sulfide globules represent a quenched sulfide melt that segregated from the picritic melt (Fig. 6). The homogenous composition of all the phases (Table 2) attests the attainment of equilibrium. Our experiments, conducted at oxygen fugacities between QFM -0.8 and QFM +2.1, explore the most oxidizing condition of the existing experimental database (Fig. 7; Fleet



and MacRae 1988; Gaetani and Grove 1997; Brennan and Caciagli 2000; Brennan 2003).

The sulfides present Ni tenor from 0.8 to 7 wt.%, which are lower than previous data (Fig. 7). The  $K_D$  of Fe–Ni equilibrium between sulfide and coexisting olivine vary from 2.9 to 10.7, and are also among the lowest values of the dataset.

### *Sulfide melt compositions of the Permian Ni–Cu deposits*

#### Compositional variation of pentlandite

It is necessary to determine the Ni content of pentlandite in order to determine the Ni tenor of the natural sulfide melts by the method applied here. The Ni and Fe contents in pentlandite range widely from deposit to deposit (Table 3). Pentlandite from the Kalatongke and Tudun deposits contain the highest Ni contents (35–37 wt.%) and lowest Fe contents (28–30 wt.%) of all the Ni–Cu deposits in NW China, with Ni/Fe ratios varying from 1.16 to 1.32. In contrast, pentlandite from the Poyi intrusion has relatively low Ni contents (27.5–32.5 wt.%) and high Fe contents (32.6–37.4 wt.%), with Ni/Fe ratios varying from 0.73 to 1. Other deposits, such as the Huangshanxi, Huangshandong, Huangshannan, and Xiangshanzhong, have medium Fe and Ni contents (29–32 wt.% and 32–34.5 wt.%, respectively) and Ni/Fe ratios (1.01–1.17) in pentlandite. In addition to Fe and Ni contents, Co contents in pentlandite vary significantly, from 0.6 to 0.9 wt.% at the Poyi and Huangshannan deposits and from 1.3 to 2.5 wt.% at other deposits.

Nickel and Cu tenors in sulfide melt

The Ni tenors of sulfides in the Poyi deposit (Table 4), estimated from XRF images at both thin section and hand sample scales (Fig. 8), vary from 13.1 to 16 wt.%, which is significantly higher than the estimate (average value of 8 wt.%) by Yang et al. (2014) and slightly higher than the estimate (average value of 12 wt.%) by Xue et al. (2016). The Ni tenors estimated by the previous studies are based on the whole rock Ni, Cu, S concentrations. The inconsistency in Ni tenor yielded from these two methods is probably due to the uncertainty of the correction of background Ni in olivine when using the method based on whole rock S, Ni, and Cu contents. Since the mineralization in the Poyi deposit is characterized by high proportion of olivine and low proportion of sulfide (large proportion of mineralization contain less than 2 wt.% S contents), the error of Ni tenors calculated by whole rock composition for these rocks may be extremely high as pointed out by Barnes et al. (2011), owing to the fact that at small sulfide proportions large uncertainties in the silicate Ni background are amplified into very large uncertainties in the sulfide tenor. This component of uncertainty is avoided by the direct sulfide mode measurement technique employed here. Our XRF results of the sulfide compositions from the Poyi deposit show that these sulfides are comparable with the high Ni tenor sulfides in the Huangshannan deposit (Mao et al. 2017). The comparison suggests that the XRF images potentially provide a better way to calculate Ni tenor for low-grade ores associated with high proportions of olivine.

The Ni tenors of samples from other deposits are well consistent with the published

data calculated from whole rock concentrations (Table 4). In contrast to the high Ni tenor characteristic of the Huangshannan and Poyi deposits which contain high Ni/Cu (2.5 to 7.3) but low Fe/Ni ratios ( $\sim 3$ ), sulfides from the Huangshanxi, Huangshandong, Xiangshanzhong, Tudun, Tianyu, Hulu, and Tulaergen deposits have intermediate Ni tenors (4–8.8 wt.%), Ni/Cu (0.9–2.5) and Fe/Ni (5.7–14) ratios. The sulfides from the Kalatongke deposit are dominated by low Ni ( $\sim 3.4$  wt.%) but high Cu ( $\sim 6.1$  wt.%) tenors, with Ni/Cu and Fe/Ni ratios varying from 0.1 to 0.9 and 15 to 38, respectively. No systematic correlation is observed between Ni content in pentlandite and Ni tenor in bulk sulfide, but the Ni/Co ratios of the Poyi and Huangshannan deposits (high Ni tenor, shown below) are higher than 30, whereas those from other deposits (reduced Ni tenor) are commonly less than 30.

#### *Olivine composition of the Permian Ni–Cu deposits*

Olivines in sulfide barren samples show a positive correlation between Fo value and Ni tenor for the Ni–Cu deposits in NW China. Differently, olivines in mineralized samples tend to show a negative correlation, such as the Poyi, Huangshannan, Xiangshanzhong, Huangshanxi, and Kalatongke deposits (Fig. 9a), indicating significant Fe–Ni exchange between sulfide and olivine. This negative correlation arises during closed-system equilibration where most of the Ni in the system is in sulfide; hence, as the Fe content of the olivine increases during reaction with trapped liquid, the Ni content of the olivine also increases to satisfy the Fe–Ni exchange  $K_D$

from equation 1 (Barnes and Naldrett 1985; Li et al. 2003).

Nevertheless, there is little difference in Fo variation between olivine from the sulfide-bearing rocks and these from the sulfide-barren rocks. For clarity, we use the average olivine composition for each deposit to the further comparison (Fig. 9b). Generally, the Permian deposits have Fo values varying from 88 to 76.5 (Table 5). The Huangshannan deposit in the North Tianshan and Poyi deposit from the Beishan Terrane have relatively high Fo values (85.9–88 mol.%) and high Ni contents (2300–2800 ppm), suggesting these deposits were formed by relatively unfractionated magmas. On the other hand, the Kalatongke and Xiangshanzhong intrusions contain low Fo values (76–79.5 mol.%) and relatively low Ni contents (1000–1300 ppm), illustrating the parental magmas of these deposits are relatively evolved. The olivines from the Huangshandong, Huangshanxi, Tudun, Tulaergen, Hulu, and Tianyu deposits contain moderate Fo values (80–83.4) but variable Ni contents (670 to 1400 ppm). The olivines from the Hulu and Tianyu deposits (intermediate Fo values, 80.4 and 83.4) are significantly lower in Ni (average values of 780 and 600 ppm, respectively) than other deposits.

There is a good positive correlation between Fo values in olivine and Ni tenor in sulfide for these deposits, except the Huangshannan and Tulaergen deposits which contain relatively higher Ni tenors than these having similar Fo values (Fig. 10). A positive correlation is also evident between Ni in olivine and Ni in sulfide, the Kalatongke low Ni tenor deposit being slightly outside of the main trend (Fig. 11a).

Commonly, high Ni tenor sulfides are associated with olivines with high Fo values ( $>86$ ) and Ni contents ( $>2000$  ppm). In addition, the Fe/Ni ratios in olivine ( $<50$ ) from the high Ni tenor deposits are significantly lower than those from the relatively low Ni tenor deposits ( $>80$ ) (Fig. 11b). The Cu/Ni ratios in sulfide tend to be higher than 1 for deposits consisting of olivine Fo values lower than 80, whereas Cu/Ni ratios are generally lower than 1 for deposits with olivine Fo values higher than 80 (Fig. 11c). The calculated exchange coefficient  $K_D$  of Fe–Ni equilibrium between sulfide and coexisting olivine of the Permian Ni–Cu deposits varies from 7.3 to 21.8 (Fig. 12). The  $K_D$  values of the Kalatongke, Huangshandong, Tudun, and Poyi deposits ( $K_D < 13$ ) are slightly lower than these from the Huangshanxi, Tulaergen, Xiangshanzhong, Hulu, and Tianyu deposits ( $K_D > 13$ ). The Kalatongke deposit in the East Junggar contains the lowest  $K_D$  and Ni tenor in sulfide, making it distinctly different from other coeval Ni–Cu deposits in east Tianshan (Tables 4, and 5, Figs. 11, and 12).

## Discussion

*Empirical equations to estimate the oxygen fugacity of sulfide– and olivine–saturated magmas*

The equilibrium constant for the exchange of Fe and Ni between coexisting olivine and sulfide liquid ( $K_D$ ) has been investigated in a number of experimental studies (Brenan 2003; Brenan and Caciagli 2000; Fleet and MacRae 1988; Gaetani and Grove

1997). In terms of the systematic dependence of  $K_D$  on  $fO_2$ , Ni tenor in sulfide ( $C_{Ni}$ ), and in some case  $fS_2$ , several empirical equations of  $K_D$ ,  $fO_2$ ,  $C_{Ni}$  have been proposed (Barnes et al. 2013; Brenan and Caciagli 2000; Sciortino et al. 2015). Brenan and Caciagli (2000) used a larger experimental database relative to previous studies (Fleet and MacRae 1988; Gaetani and Grove 1997) and found the relationship between  $K_D$  and  $\log(fO_2)$  to be best described by a power-law relation. Barnes et al. (2013), using the same experimental dataset, made the equation more applicable to model calculations by replacing the  $\log(fO_2)$  by  $\Delta QFM$  ( $fO_2$  relative to the quartz-fayalite-magnetite oxygen buffer) and developed a polynomial equation relating  $K_D$  to  $C_{Ni}$  (including a cubic term) and  $\Delta QFM$ . This equation enables estimation of the oxygen fugacity of the magma relative to QFM buffer, which is independent of the temperature. Recently, Sciortino et al. (2015) recalibrated the same data set using only a linear term for  $C_{Ni}$ , but also introducing a term for  $fS_2$ :

$$K_D = C_{Ni} \cdot [34.7 \cdot \log(fO_2 / fS_2) + 312] - 11 \cdot \log(fO_2 / fS_2) - 70.8 \quad (2)$$

the revised equation (2) can well predict the  $fO_2$  of the parental magma but requires an estimate of  $fS_2$  which is dependent on the silicate melt composition, equilibrium temperature, and pressure. This formulation requires a complex parameterization of these dependencies in order to obtain a solution, and is therefore difficult to access in natural systems. Furthermore, this equation fails to apply to the new data in this study (Fig. 13), when  $fS_2$  is calculated using the equation in Mungall and Brenan (2014).

We added some new experimental data (Table 2) to the currently published dataset

(Brenan 2003; Brenan and Caciagli 2000; Fleet and MacRae 1988; Gaetani and Grove 1997) to calibrate a linear  $C_{Ni}$  and  $\Delta QFM$  dependent equation for  $K_D$ . Our new experimental data using a picritic gabbro–dolerite as starting material represent the lowest Ni tenor in sulfide (1.5–1.8 wt.%), and the most oxidizing conditions (from QFM –0.78 to QFM +2.11) in the database (Table 2). The ultra–high  $K_D$  values (>40), which are commonly relating to ultra–high Ni content in sulfide (>50 wt.%), were not included in our calibration because of the poor linear relationship (Fig. 7). This will not influence the application of this equation to magmatic Ni–Cu systems due to the rarity of such compositions in nature. The relationship among  $K_D$ , sulfide melt compositions, and calculated  $\Delta QFM$  was evaluated by multivariate linear regression analysis and is given by:

$$K_D = a + b \cdot C_{Ni} + c \cdot \Delta QFM \quad (3)$$

In this equation, a, b, and c are constants which equal to 9.775, 0.416, and –4.308, respectively. The standard deviation of these constants is listed in Table 6 and the comparison of predicted  $K_D$  values between this equation and previous equations is present in Fig. 13. The average relative error of prediction for  $K_D$  using equation (3) is  $\pm 17.7\%$  for all the data, similar to that of the equation (2) for the old data ( $\pm 18.2\%$ ). The average error of prediction for  $\Delta QFM$  using equation (3) is  $\pm 0.8$  log unit  $\Delta QFM$  for all the data.

475 *Application of the empirical oxygen fugacity equation to the Permian Ni–Cu deposits*  
476 *in southern Central Asian Orogenic Belt*

477 In the following discussion, the term “host magma” is used to represent the magma  
478 that was initially emplaced to form each individual intrusion, before in-situ  
479 fractionation within the intrusion, this term being equivalent to the term “parental  
480 magma” used in previous studies (Mao et al. 2015; Mao et al. 2014a; Sun et al. 2013b).  
481 Here we use “parental magma” to denote the most primitive host magma of the entire  
482 suite of Ni–Cu deposits in NW China, i.e. the magma that undergone the least  
483 fractionation and contamination after leaving the mantle source (primary magma).

484 The reverse correlations between Fo value and Ni content in olivine from  
485 mineralized samples (Fig. 9a) show that equilibrium of Fe and Ni exchange between  
486 olivine and sulfide were reached for the Permian Ni–Cu deposits. Based on the sulfide  
487 composition and  $K_D$  values of the sulfide bearing samples (Table 4), the  $\Delta QFM$  values  
488 of the host magmas that were in equilibrium with sulfides (Fig. 14) were estimated  
489 using equation (3). Only samples with integrated olivine and sulfide compositions were  
490 used in the estimation. The samples which have undergone significant sulfide  
491 fractionation, i.e. anomaly Cu/Ni ratio (Table 4), were excluded from the oxygen  
492 fugacity calculation. For the Tianyu and Hulu deposit, which have no integrated olivine  
493 and sulfide compositions, the average composition of sulfides and olivine in  
494 disseminated to net-textured ores of these deposits were used to estimate the oxygen  
495 fugacity. The variations in oxygen fugacity of these two deposits are illustrated as error



bar, which is resulted from the variation in compositions of olivine and sulfides of these deposits. The Poyi, Huangshannan, and Kalatongke intrusions were found to be associated with the most oxidizing magmas in NW China, with oxygen fugacity at around QFM +1. On the other hand, the other deposits (the Tianyu, Xiangshanzhong, Tulaergen, and Huangshanxi deposits) are associated with relatively reduced magma with  $fO_2$  varying from QFM -2 to QFM +0.3. In the plot of  $\Delta QFM$  values versus Fo values in olivine (Fig. 14), the oxidation state of the host magma of the deposits in east Tianshan decreases as the Fo values decrease, indicating that these host magmas became gradually more reduced during the evolution.

#### *Origin of the oxygen fugacity variation in the host magmas*

Note that the ranges of  $fO_2$  for individual deposit are commonly within one log unit QFM, but the range of the  $fO_2$  in the Huangshanxi deposit is significantly larger, varying from ~QFM +1 to ~QFM -2. The extremely reducing oxidation state recorded in the sample 06-18-944.3 (QFM -2) is not caused by sulfide fractionation (Table 4). The high V/Sc and V/Ga ratios and heavy oxygen isotope enrichment in olivine of the sample 06-18-944.3 relative to those of other samples in the Huangshanxi deposit (Mao et al., in preparation) strongly suggest that the extremely reducing oxidation state in sample 06-18-944.3 is the result of significant assimilation of graphite-bearing wall rock. Furthermore, the relatively high oxidation state recorded in the Poyi and Huangshannan Ni-Cu deposits, containing the most primitive olivines (Fo values

516 higher than 86 mol.%), suggests that the primitive magmas of these deposits are  
517 characterized by relatively oxidizing condition. Such oxidation state of magmas is  
518 consistent with that of spinel peridotites of the mantle wedge above the subduction zone,  
519 which have oxygen fugacity of QFM +0.3 to QFM +2.0 (Frost and McCammon 2008;  
520 Parkinson and Arculus 1999). The fact that all of these Permian deposits are  
521 characterized by compositions of subduction zone affinity, i.e. significantly Nb and Ta  
522 depletion relatively to Th and La, positive Pb and Sr anomalies (Deng et al. 2015; Li et  
523 al. 2012; Mao et al. 2014a; Mao et al. 2016; Su et al. 2011), suggests that the magmas  
524 were derived from extensively metasomatized supra-subduction zone mantle sources,  
525 which may melt to form relative oxidizing magmas. Fractional crystallization modeling  
526 of the host magma of the Poyi and Huangshannan deposits (Xue et al., 2016; Mao et  
527 al., 2016) using MELTS (Asimow and Ghiorso 1998) predicts that the redox state of  
528 these host magmas during olivine plus Cr-spinel fractionation should increase slightly  
529 from QFM +1.2 to QFM +1.4, and from QFM +0.7 to QFM +1, respectively, at 1 kbar  
530 pressure condition. The modeling results indicate that the fractionation is not the cause  
531 of the progressive reduction for the fractionated host magmas. On the other hand, our  
532 observed trend towards more reduced magmas with increasing fractionation (Fig 14) in  
533 the east Tianshan intrusions could be the result of interaction with the relatively reduced  
534 crustal materials. The assimilation of small amounts of organic matter (<1 wt.%) by  
535 mafic-ultramafic magmas may dramatically decrease magma redox conditions (Iacono-  
536 Marziano et al., 2012; 2017). For instance, the sulfide saturation of the parent magmas

to the Noril'sk–Talnakh Ni–Cu–PGE deposits is believed to have been triggered by contamination of evaporite-bearing country rocks and organic matter from the country rocks (Grinenko 1985; Li et al. 2003; Naldrett 2004; Iacono-Marziano et al. 2017). The addition of evaporite increased the sulfate content of the parental magma, whereas the input of reducing agents decreased the oxygen fugacity of the magma and reduced this sulfate to much less soluble sulfide. In addition, in light of both isotopic and petrographic evidence of the Voisey's Bay magmatic system (QFM–1 to QFM –3), a model of magma reduction involving assimilation of graphite-bearing country rock by a relatively oxidized parental magma has been explored (Brenan and Li 2000). The ubiquitous occurrence of graphite-bearing tuff and graphite-bearing slate in the Carboniferous wall rock of most of the mafic–ultramafic intrusions in the North Tianshan and East Junggar terranes (Table 1, Fig. 2) may provide the reducing agents to the magmas. The presence of xenolith of graphite-bearing wall rock in the Huangshandong, Huangshannan and Huangshanxi intrusion (Wang et al., 1987) suggests that the addition of carbonaceous material took place in these magmatic systems. Thus, Ni–Cu deposits in the North Tianshan and the Beishan Terrane could be the result of derivation from relatively oxidizing mantle source and became gradually more reduced during the interaction with the wall rock. However, the absence of graphite-bearing wall rocks in the Central Tianshan (Table 1) illustrates that the relatively reduced feature of the Tianyu deposit is either the result of a relatively reduced mantle source or addition of reducing agent to an oxidized magma at depth.

The latter scenario is possible due to the presence of Pre-Cambrian black shales in the Central Tianshan Terrane (Table 1, Yang 2015).

Our observations raise the question of whether the addition of reducing agents is necessary to trigger immiscible sulfide saturation in subduction-associated settings. The  $fO_2$  range controls sulfur speciation and hence maximum sulfur contents in the magma during both source melting and sulfide segregation at the shallow crust, especially for magmas generated in the arc, backarc, and island arc settings (Jugo 2009). During low degree source partial melting, significantly oxidizing circumstances could generate sulfide undersaturated primitive magma which may contain extremely high S content as well as metal contents (such as PGE), because no sulfide in the mantle holds PGE in the source and most PGE will dissolve into the magma. When such relatively oxidizing magma arrives at the shallow magma chamber, more reduced conditions are required to segregate sulfide rather than sulfate from the magma. This scenario was postulated by Deng et al. (2014) and Zhao et al. (2016), who proposed that graphite assimilation may play a critical role in causing sulfide segregation in the Ni–Cu deposits in NW China. However, there is no reason to invoke an extremely high  $fO_2$  ( $> QFM +2$ ) for the mantle source as well as the primary magma of the Permian deposits. Partial melting of such source would generate PGE rich magmas, but no sign of PGE rich magma has been observed in these deposits; the opposite is true in that the host magmas to all the intrusions appear to be PGE depleted (Li et al., 2012; Zhang et al., 2011; Mao et al., 2014a; Xue et al., 2016). Moreover, even in the Poyi intrusion, which was formed by

the most oxidized magma of the deposits in NW China, the oxygen fugacity is still within the range where most of the S is dissolved as sulfide rather than sulfate. The reduction accompanying the differentiation of the parental magma (Fig.14) does not seem to be due to fractional crystallization and therefore suggests the assimilation of graphite and sulfur bearing crustal material that also introduced the extra S to trigger sulfide saturation.

#### *Origin of the variation in Ni tenor in sulfide*

The Ni content and the Fo value in olivine are related to Ni content and Mg/Fe values in the magma from which the olivines are crystallized by partition coefficients, which have been experimentally determined (Kiseeva and Wood 2013; Naldrett 2004; Roeder and Emslie 1970) and therefore can be used to infer composition of the magma. The spread of Fo values in olivine from the Ni–Cu deposits in NW China (Fig. 9) illustrates that these deposits are associated with magmas containing different Fe/Mg ratios and Ni contents, which are consistent with the previous estimation of host magma compositions using Fe/Mg equilibrium between olivine and silicate liquid (Li et al. 2012; Mao et al. 2014a; Mao et al. 2016; Xue et al. 2016).

On the basis that these Permian deposits in the east Tianshan were emplaced in a similar crustal architecture and derived from the similar mantle source, probably relating to the same event (Qin et al. 2011; Song et al. 2013; Su et al. 2011), we treat the host magma of the Poyi intrusion, which has the highest Fo value in olivine and has

599 experienced only weak crustal contamination (Yang et al. 2014), as the parental magma  
 600 to model its fractionation process. In our modeling, olivine composition is calculated at  
 601 each step using the well-established Roeder and Emslie (1970) relationship for the  
 602 Mg/Fe  $K_D$  between olivine and silicate melt ( $K_D = (\text{FeO/MgO})_{\text{Olivine}}/(\text{FeO/MgO})_{\text{Liquid}}$   
 603  $=0.3$ ). The residual magma compositions were estimated by subtracting the component  
 604 in olivine from the parental magma. The Ni content in the residual melt is calculated  
 605 from the Rayleigh fractional crystallization equation and the partitioning value of Ni  
 606 between less fractionated olivine ( $\text{Fo}>80$ ) and magma ( $D_{\text{ol-magma}}$ ) was estimated using  
 607 the composition based equation of Li and Ripley (2010) (Table 7). The partitioning  
 608 values of Ni between olivine and magma for the highly fractionated olivines were  
 609 assumed as 13 for olivine of  $\text{Fo}_{78}$  and 17 for olivine of  $\text{Fo}_{74}$  (See summary in Li and  
 610 Ripley, 2010). The olivine crystallized from more reducing magma will have higher  
 611 fayalite during reduce  $\text{Fe}^{3+}$  to  $\text{Fe}^{2+}$ , MELTS modeling indicates that change of one log  
 612 unit oxidation state of the magma will cause  $\sim 2$  mol.% variation of Fo value in olivine,  
 613 which is easily within the range of variability that would be expected from trapped  
 614 liquid reactions (30% trapped liquid, Fig. 9b) (Barnes 1986). Thus, the oxygen fugacity  
 615 of the parental magma and the residual melts during fractionation were set as QFM +1  
 616 for simplicity. The olivine composition of most of the Ni–Cu deposits plots along the  
 617 olivine fractionation model line (Fig. 9), demonstrating their host magmas were formed  
 618 by a variable degree of olivine fractionation in depth by the parental magma. The  
 619 relative low Ni content in olivine recorded by the Hulu, Huangshanxi, and Tianyu

620 deposits could be the result of sulfide segregation along with olivine fractionation at  
621 depth. The olivine compositions of the Kalatongke deposit in the East Junggar was also  
622 plotted for comparison, although it is most likely belonged to a different system and  
623 could derive from a different parental magma. Olivine composition from the  
624 Kalatongke deposit are all plotted above the modelling line, also away from the trend  
625 for the trapped liquid effect (Fig. 9b), but can be the result of olivine fractionation at  
626 the beginning (0–15%) plus subsequent olivine+clinopyroxene+plagioclase  
627 fractionation at 5:4:1 (Fig. 9b). Since Ni is compatible and Cu is incompatible in olivine,  
628 olivine fractionation of the parental magma decreases the Ni content and increase the  
629 Cu/Ni ratio in the evolved magmas; thus sulfides segregated from the more fractionated  
630 magma will be depleted in Ni and enriched in Cu/Ni ratio relative to these segregated  
631 from the less fractionated parental magmas. The observations that Ni tenor in sulfide  
632 decreases with Fo value in olivine (Fig. 10) and Cu/Ni ratio in sulfide increases with  
633 decrease of Fo value in olivine (Fig. 11c) are consistent with an interpretation that  
634 sulfides from the Ni–Cu deposits in NW China were segregated from similar parental  
635 magmas that have experienced variable degree of olivine fractionation. R-factor model  
636 using the Ni concentration in the residual silicate melts and calculated  $D_{Ni}$  between  
637 sulfide and silicate from the equation of Kiseeva and Wood (2013), indicates that these  
638 sulfides were segregated from variable R value, varying from 300 to 7000 (Fig. 10,  
639 Table 7). The Poyi deposit is characterized by high R value (1000-7000), which is  
640 significantly higher than other deposits (200-3000). The enrichment of Ni tenor in

sulfide of the Huangshannan and Tulaergen deposits relative to other Ni–Cu deposits with similar Fo value in olivine (Fig. 10) may be the result of extra Ni sequestered from olivine via open–system olivine–sulfide–silicate melt equilibrium (Fig. 9a) (Barnes et al. 2013; Mao et al. 2017). In summary, the variation in Ni tenor in sulfides from the east Tianshan Ni–Cu deposits is controlled by variable R-values and host magma compositions that have been derived from the various degree of olivine fractionation before the final emplacement. Relatively high Ni tenor in sulfide may be a consequence of equilibration with olivine-phyric magmas.

#### *A genetic model for the Ni–Cu deposits in NW China*

A genetic model of the Permian Ni–Cu deposits in east Tianshan is illustrated in Fig. 15. The low and variable degree of partial melting of supra-subduction zone mantle gave rise to the primary magmas, which have high Ni and relatively low PGE concentrations. After (5–10 %) olivine fractionation during ascent, the mafic magmas entrained immiscible sulfide due to sulfide assimilation in the crust (Mao et al. 2016; Xia et al. 2013; Xue et al. 2016; Yang et al. 2014). These sulfide-loaded melts got emplaced into dike and dike–keel like structural traps, in which sulfides interacted with a variable amount of silicate melts, giving rise to high Ni and relatively high PGE tenor sulfides, such as the Huangshannan and Poyi deposits (Fig. 15a). These magmas had relatively high oxygen fugacity ( $\sim$ QFM +1), reflecting a supra-subduction zone mantle source and implying limited interaction with reduced country rocks. Some of the



mantle-derived magmas experienced a larger amount of olivine fractionation (15–20%) at depth, reducing the Ni concentration but without greatly changing the PGE concentrations, giving rise to magmas with decreased Ni contents. Meanwhile, the differentiated magma becoming increasingly reduced due to contamination with reduced (presumably graphite) country rocks, during which immiscible sulfide segregated from the magma and became entrained in the magma flow. These sulfide-loaded magmas gave rise to deposits with reduced Ni tenors and relatively reducing oxidation state ( $-2 < \Delta QFM < 0$ ) in the form of conduits, sills, and chonoliths (Fig. 15b). These moderate Ni tenor deposits comprise the Huangshandong, Huangshanxi, Xiangshanzhong, Tudun, and Tulaergen deposits.

The Kalatongke deposit in the East Junggar probably belongs to a different system compared to the Ni–Cu deposits occur in the east Tianshan. The relatively oxidizing nature of the Kalatongke magma, together with the wide presence of graphite-bearing wall rock and a high degree of crustal contamination, suggests that the parental magma, probably as well as its mantle source, are even more oxidized. The low Ni tenor in sulfide could be the result of significant olivine fractionation during ascent. Significant fractionation ( $>20\%$ , olivine, clinopyroxene, and plagioclase) of the mantle melts without substantially reducing material addition generated mildly oxidized magmas ( $\sim QFM +1$ ) containing relatively low Ni concentrations and high Cu/Ni ratios. Emplacement of these evolved magmas formed the Kalatongke deposit (Fig. 15c) which has the highest Cu tenor and lowest Ni tenor among the Ni–Cu deposits in NW

China. Subsequently, significant MSS fractionation during sulfide percolation or backward flow (Barnes et al. 2016) gave rise to the sulfides with variable Ni, Cu and PGE tenors in the Kalatongke and Huangshandong mafic unit (Mao et al. 2015; Qian et al. 2009; Song and Li 2009).

## Conclusions

The exchange of Fe and Ni between coexisting olivine and sulfide liquid (KD) serves as a monitor of oxygen fugacity, which can be estimated from the recalibrated equation in this study. The calculated oxygen fugacity values of the Permian Ni–Cu deposits in the CAOBS, varying from QFM – 2 to ~QFM + 1, could be the result of the progressive interaction of originally mildly oxidized magmas with reducing crustal agents. Desktop microbeam XRF scanning is a useful tool to estimate the 100% sulfide composition for magmatic Ni–Cu deposits, especially for samples with low Ni grade and a high proportion of background Ni. The Permian Ni–Cu deposits in the CAOBS exhibit a wide range of Ni content in sulfide varying from ~3 to 16 wt% at the deposit scale. The variation in Ni tenor in sulfide of these deposits is the result of sulfide segregation from magmas with variable Ni contents. The magmatic Ni–Cu system in the East Tianshan was formed by host magmas that experienced a variable amount of olivine fractionation associated with assimilation of reduced country rock at depth. The Kalatongke deposit in the East Junggar with low Ni content in sulfide (< 5 wt%) and high Cu/Ni ratio was formed by a host magma that experienced significant pre

703 emplacement olivine fractionation. Fractional crystallization and crustal assimilation  
704 played important roles in giving rise to the variability of Ni content in sulfide and  
705 oxygen fugacity in the Ni–Cu deposits in the CAOBS.

## 707       **Acknowledgements**

708       This study has been financially supported by grants from the National Key  
709 Research and Development Program of China (2017YFC0601204), the National  
710 Natural Science Foundation of China (41502095), the French agency for research  
711 (ANR project #12JS06-0009-01), and China Postdoctoral Science Foundation  
712 (2015M570146 Ya–Jing Mao). Xinjiang Nonferrous Metal Industry Group Ltd. is  
713 thanked for access to the Ni–Cu deposits in NW China. Xue–Jun Yan, Jun–Hui Xie,  
714 Yong Wang, Bin Wang, Guan–Liang Ren, Ding–Min Guo, and Yu–Zong Liang are  
715 thanked for their sharing of knowledge of the deposits in the field work. The assistance  
716 of Ida Di Carlo and Patricia Benoist-Julliot with the SEM and the electron microprobe  
717 in Orléans is acknowledged. Guohui Chen, Tongcheng Han, and Na Guo are  
718 acknowledged for their help on best-fit calibration for the experimental data. Ya–Jing  
719 Mao acknowledges the funding of the China Scholarship Council to support the visit to  
720 CSIRO as a postdoctoral fellow. SJB acknowledges support from the CSIRO Science  
721 Plus Science Leader program. Valuable comments from Margaux Le Vaillant, Sheng-  
722 Hong Yang, and Chusi Li improved the manuscript. Editors Wolfgang Maier and Bernd  
723 Lehmann are acknowledged for their helpful suggestions and editorial handling.

724 **References**

- 725 Asimow PD, Ghiorso MS (1998) Algorithmic modifications extending MELTS to  
726 calculate subsolidus phase relations. *Am Mineral* 83:1127-1132
- 727 Barnes SJ (1986) The effect of trapped liquid crystallization on cumulus mineral  
728 compositions in layered intrusions. *Contrib Mineral Petr* 93:524-531  
729 doi:10.1007/BF00371722
- 730 Barnes SJ, Naldrett AJ (1985) Geochemistry of the J-M (Howland) Reef of the  
731 Stillwater Complex, Minneapolis Adit area; I, Sulfide chemistry and sulfide-  
732 olivine equilibrium. *Econ Geol* 80:627-645 doi:10.2113/gsecongeo.80.3.627
- 733 Barnes SJ, Cruden AR, Arndt N, Saumur BM (2016) The mineral system approach  
734 applied to magmatic Ni–Cu–PGE sulphide deposits. *Ore Geol Rev* 76:296-316  
735 doi:http://dx.doi.org/10.1016/j.oregeorev.2015.06.012
- 736 Barnes SJ, Godel B, Gürer D, Brenan JM, Robertson J, Paterson D (2013) Sulfide-  
737 Olivine Fe-Ni Exchange and the Origin of Anomalously Ni Rich Magmatic  
738 Sulfides. *Econ Geol* 108:1971-1982 doi:10.2113/econgeo.108.8.1971
- 739 Barnes SJ, Osborne GA, Cook D, Barnes L, Maier WD, Godel B (2011) The Santa Rita  
740 Nickel Sulfide Deposit in the Fazenda Mirabela Intrusion, Bahia, Brazil:  
741 Geology, Sulfide Geochemistry, and Genesis. *Econ Geol* 106:1083-1110  
742 doi:10.2113/econgeo.106.7.1083
- 743 BGMRXUAR (Bureau of Geology and mineral Resources of Xinjiang Uygur  
744 Autonomous Region) (1993) Regional Geology of Xinjiang Uygur

745 Autonomous Region. Geological Publishing House, Beijing, 1-841

746 Botcharnikov R, Almeev R, Koepke J, Holtz F (2008) Phase relations and liquid lines  
 747 of descent in hydrous ferrobalt—implications for the Skaergaard intrusion and  
 748 Columbia River flood basalts. *J Petrol* 49:1687-1727

749 Brenan JM (2003) Effects of  $fO_2$ ,  $fS_2$ , temperature, and melt composition on Fe-Ni  
 750 exchange between olivine and sulfide liquid: implications for natural olivine–  
 751 sulfide assemblages. *Geochim Cosmochim Acta* 67:2663-2681  
 752 doi:10.1016/s0016-7037(02)01416-3

753 Brenan JM, Caciagli NC (2000) Fe–Ni exchange between olivine and sulphide liquid:  
 754 implications for oxygen barometry in sulphide-saturated magmas. *Geochim  
 755 Cosmochim Acta* 64:307-320 doi:http://dx.doi.org/10.1016/S0016-  
 756 7037(99)00278-1

757 Brenan JM, Li C (2000) Constraints on Oxygen Fugacity during Sulfide Segregation in  
 758 the Voisey's Bay Intrusion, Labrador, Canada. *Econ Geol* 95:901-915  
 759 doi:10.2113/gsecongeo.95.4.901

760 Chai F, Zhang Z, Mao J, Dong L, Zhang Z, Wu H (2008) Geology, petrology and  
 761 geochemistry of the Baishiquan Ni–Cu-bearing mafic–ultramafic intrusions in  
 762 Xinjiang, NW China: Implications for tectonics and genesis of ores. *J Asian  
 763 Earth Sci* 32:218-235 doi:http://dx.doi.org/10.1016/j.jseaes.2007.10.014

764 Deng Y-F, Song X-Y, Chen L-M et al. (2014) Geochemistry of the Huangshandong Ni–  
 765 Cu deposit in northwestern China: Implications for the formation of magmatic

766 sulfide mineralization in orogenic belts. *Ore Geol Rev* 56:181-198  
 767 doi:10.1016/j.oregeorev.2013.08.012  
 768 Deng Y-F, Song X-Y, Hollings P, Zhou T, Yuan F, Chen L-M, Zhang D (2015) Role of  
 769 asthenosphere and lithosphere in the genesis of the Early Permian Huangshan  
 770 mafic-ultramafic intrusion in the Northern Tianshan, NW China. *Lithos*  
 771 227:241-254 doi:http://dx.doi.org/10.1016/j.lithos.2015.04.014  
 772 Fleet ME, MacRae ND (1988) Partition of Ni between olivine and sulfide: equilibria  
 773 with sulfide-oxide liquids. *Contrib Mineral Petr* 100:462-469  
 774 doi:10.1007/bf00371375  
 775 Frost DJ, McCammon CA (2008) The Redox State of Earth's Mantle. *Annual Review*  
 776 of Earth and Planetary Sciences 36:389-420  
 777 doi:doi:10.1146/annurev.earth.36.031207.124322  
 778 Gaetani GA, Grove TL (1997) Partitioning of moderately siderophile elements among  
 779 olivine, silicate melt, and sulfide melt: constraints on core formation in the Earth  
 780 and Mars. *Geochim Cosmochim Acta* 61:1829-1846  
 781 Gao J-F, Zhou M-F (2013) Generation and evolution of siliceous high magnesium  
 782 basaltic magmas in the formation of the Permian Huangshandong intrusion  
 783 (Xinjiang, NW China). *Lithos* 162:128-139 doi:DOI  
 784 10.1016/j.lithos.2013.01.002  
 785 Gao JF, Zhou MF, Lightfoot PC, Wang CY, Qi L (2012) Origin of PGE-Poor and Cu-  
 786 Rich Magmatic Sulfides from the Kalatongke Deposit, Xinjiang, Northwest

787 China. *Econ Geol* 107:481-506 doi:10.2113/econgeo.107.3.481

788 Grinenko L (1985) Sources of sulfur of the nickeliferous and barren gabbro-dolerite  
 789 intrusions of the northwest Siberian platform. *Int Geol Rev* 27:695-708

790 Han BF, Ji JQ, Song B, Chen LH, Li Z (2004) SHRIMP zircon U-Pb ages of kalatongke  
 791 No. 1 and Huangshandong Cu-Ni-bearing mafic-ultramafic complexes, North  
 792 Xinjiang, and geological implications. *Chinese Sci Bull* 49:2424-2429 doi:Doi  
 793 10.1360/04wd0163

794 Han CM, Xiao WJ, Zhao GC, Ao SJ, Zhang JE, Qu WJ, Du AD (2010) In-situ U-Pb,  
 795 Hf and Re-Os isotopic analyses of the Xiangshan Ni-Cu-Co deposit in Eastern  
 796 Tianshan (Xinjiang), Central Asia Orogenic Belt Constraints on the timing and  
 797 genesis of the mineralization. *Lithos* 120:547-562 doi:DOI  
 798 10.1016/j.lithos.2010.09.019

799 Han C, Xiao W, Zhao G et al. (2013) SIMS U-Pb zircon dating and Re-Os isotopic  
 800 analysis of the Hulu Cu-Ni deposit, eastern Tianshan, Central Asian Orogenic  
 801 Belt, and its geological significance. *Journal of Geosciences* 58:251-270

802 Iacono-Marziano G, Gaillard F, Scaillet B, Polozov AG, Marecal V, Pirre M, Arndt NT  
 803 (2012) Extremely reducing conditions reached during basaltic intrusion in  
 804 organic matter-bearing sediments. *Earth Planet Sc Lett* 357–358:319-326  
 805 doi:http://dx.doi.org/10.1016/j.epsl.2012.09.052

806 Jahn BM (2004) The central Asian orogenic belt and growth of the continental crust in  
 807 the phanerozoic. *Geol Soc Spec Publ* 226:73-100 doi:Doi

808 10.1144/Gsl.Sp.2004.226.01.05

809 Jugo PJ (2009) Sulfur content at sulfide saturation in oxidized magmas. *Geology*

810 37:415-418 doi:10.1130/g25527a.1

811 Kiseeva ES, Wood BJ (2013) A simple model for chalcophile element partitioning

812 between sulphide and silicate liquids with geochemical applications. *Earth*

813 *Planet Sc Lett* 383:68-81 doi:http://dx.doi.org/10.1016/j.epsl.2013.09.034

814 Li C, Ripley EM (2010) The relative effects of composition and temperature on olivine-

815 liquid Ni partitioning: Statistical deconvolution and implications for petrologic

816 modeling. *Chem Geol* 275:99-104

817 doi:http://dx.doi.org/10.1016/j.chemgeo.2010.05.001

818 Li C, Ripley EM, Naldrett AJ (2003) Compositional variations of olivine and sulfur

819 isotopes in the Noril'sk and Talnakh intrusions, Siberia: Implications for ore-

820 forming processes in dynamic magma conduits. *Econ Geol Bull Soc* 98:69-86

821 Li C, Zhang M, Fu P, Qian ZZ, Hu P, Ripley EM (2012) The Kalatongke magmatic Ni-

822 Cu deposits in the Central Asian Orogenic Belt, NW China: product of slab

823 window magmatism? *Miner Deposita* 47:51-67 doi:DOI 10.1007/s00126-011-

824 0354-7

825 Li C, Zhang Z, Li W, Wang Y, Sun T, Ripley EM (2015) Geochronology, petrology and

826 Hf-S isotope geochemistry of the newly-discovered Xiarihamu magmatic Ni-

827 Cu sulfide deposit in the Qinghai-Tibet plateau, western China. *Lithos* 216-

828 217:224-240 doi:http://dx.doi.org/10.1016/j.lithos.2015.01.003



829 Li X, Wang D, Zhao S (2014) The Discovery of Baixintan Magmatic Ni-Cu Sulfide  
830 Deposits in Hami Area, Xinjiang. *Xinjiang Geology* 32:466-469

831 Lightfoot PC, Evans-Lamswood D (2015) Structural controls on the primary  
832 distribution of mafic-ultramafic intrusions containing Ni-Cu-Co-(PGE)  
833 sulfide mineralization in the roots of large igneous provinces. *Ore Geol Rev*  
834 64:354-386 doi:<http://dx.doi.org/10.1016/j.oregeorev.2014.07.010>

835 Maier W, Groves D (2011) Temporal and spatial controls on the formation of magmatic  
836 PGE and Ni-Cu deposits. *Miner Deposita* 46:841-857 doi:10.1007/s00126-011-  
837 0339-6

838 Maier WD, Smithies RH, Spaggiari CV et al. (2016) Petrogenesis and Ni-Cu sulphide  
839 potential of mafic-ultramafic rocks in the Mesoproterozoic Fraser Zone within  
840 the Albany-Fraser Orogen, Western Australia. *Precambrian Res*  
841 doi:<http://dx.doi.org/10.1016/j.precamres.2016.05.004>

842 Mao JW, Pirajno F, Zhang ZH et al. (2008) A review of the Cu-Ni sulphide deposits in  
843 the Chinese Tianshan and Altay orogens (Xinjiang Autonomous Region, NW  
844 China): Principal characteristics and ore-forming processes. *J Asian Earth Sci*  
845 32:184-203 doi:10.1016/j.jseaes.2007.10.006

846 Mao Y-J, Qin K-Z, Li C, Xue SC, Ripley EM (2014a) Petrogenesis and ore genesis of  
847 the Permian Huangshanxi sulfide ore-bearing mafic-ultramafic intrusion in the  
848 Central Asian Orogenic Belt, western China. *Lithos* 200:111-125 doi:DOI  
849 10.1016/j.lithos.2014.04.008

850 Mao Y-J, Qin K-Z, Tang D, Xue S-C, Tian Y, Feng H (2014b) Multiple phases of magma  
851 emplacement and mineralization of eastern Tianshan, Xinjiang: Exemplified by  
852 Huangshan Ni-Cu deposit. *Acta Petrol Sin* 30:1575-1594

853 Mao Y-J, Qin K-Z, Li C, Tang D-M (2015) A modified genetic model for the  
854 Huangshandong magmatic sulfide deposit in the Central Asian Orogenic Belt,  
855 Xinjiang, western China. *Miner Deposita* 50:65-82 doi:10.1007/s00126-014-  
856 0524-5

857 Mao Y-J, Qin K-Z, Tang D-M, Feng H-Y, Xue S-C (2016) Crustal contamination and  
858 sulfide immiscibility history of the Permian Huangshannan magmatic Ni-Cu  
859 sulfide deposit, East Tianshan, NW China. *J Asian Earth Sci* 129:22-37  
860 doi:http://dx.doi.org/10.1016/j.jseaes.2016.07.028

861 Mao Y-J, Qin K-Z, Barnes SJ, Tang D-M, Xue S-C, Le Vaillant M (2017) Genesis of  
862 the Huangshannan high-Ni tenor magmatic sulfide deposit in the Eastern  
863 Tianshan, northwest China: Constraints from PGE geochemistry and Os–S  
864 isotopes. *Ore Geol Rev* doi:http://dx.doi.org/10.1016/j.oregeorev.2017.05.015

865 Mungall JE, Brenan JM (2014) Partitioning of platinum-group elements and Au  
866 between sulfide liquid and basalt and the origins of mantle-crust fractionation  
867 of the chalcophile elements. *Geochim Cosmochim Ac* 125:265-289  
868 doi:http://dx.doi.org/10.1016/j.gca.2013.10.002

869 Naldrett AJ (2004) *Magmatic Sulfide Deposits: Geology, Geochemistry and*  
870 *Exploration*. Springer: 1-727

- 871 Parkinson IJ, Arculus RJ (1999) The redox state of subduction zones: insights from arc-  
872 peridotites. *Chem Geol* 160:409-423
- 873 Qian ZZ, Wang JZ, Jiang CY, Jiao JG, Yan HQ, He K, Sun T (2009) Geochemistry  
874 characters of platinum-group elements and its significances on the process of  
875 mineralization in the Kalatongke Cu-Ni sulfide deposit, Xinjiang, China. *Acta*  
876 *Petrol Sin* 25:832-844
- 877 Qin K-Z, Su B-X, Sakyi PA et al. (2011) Sm zircon U-Pb geochronology and Sr-Nd  
878 isotopes of Ni-Cu-bearing mafic-ultramafic intrusions in Eastern tianshan and  
879 Beishan in correlation with flood basalts in Tarim basin (NW china): Constraints  
880 on a Ca. 280 Ma mantle plume. *Am J Sci* 311:237-260 doi:Doi  
881 10.2475/03.2011.03
- 882 Qin K-Z, Tang D-M, Su B-X, Mao Y-J, Xue S-C (2012) The tectonic setting, style,  
883 basic feature, relative erosion degree, ore-bearing evaluation sign, potential  
884 analysis of mineralization of Cu-Ni bearing Permian mafic-ultramafic  
885 complexes, Northern Xinjiang. *Northwestern Geology* 45:83-116
- 886 Roeder PL, Emslie RF (1970) Olivine-Liquid Equilibrium. *Contrib Mineral Petr*  
887 29:275-289 doi:Doi 10.1007/Bf00371276
- 888 San J, Tian B, Lei J, Kang F, Qin K, Xu X (2003) A new discovery whole rocks  
889 mineralized Cu: Ni sulfide deposit in Tulagen, Etat Tianshan, Xinjiang. *Mineral*  
890 *Deposits* 22:270
- 891 Sciortino M, Mungall JE, Muinonen J (2015) Generation of High-Ni Sulfide and Alloy

892           Phases During Serpentinization of Dunite in the Dumont Sill, Quebec. *Econ*  
893           *Geol* 110:733-761 doi:10.2113/econgeo.110.3.733

894   Song XY, Chen LM, Deng YF, Xie W (2013) Syncollisional tholeiitic magmatism  
895           induced by asthenosphere upwelling owing to slab detachment at the southern  
896           margin of the Central Asian Orogenic Belt. *Journal of the Geological Society*  
897           170:941-950 doi:Doi 10.1144/Jgs2012-130

898   Song XY, Li XR (2009) Geochemistry of the Kalatongke Ni-Cu-(PGE) sulfide deposit,  
899           NW China: implications for the formation of magmatic sulfide mineralization  
900           in a postcollisional environment. *Miner Deposita* 44:303-327 doi:DOI  
901           10.1007/s00126-008-0219-x

902   Su B-X, Qin K-Z, Sakyi PA et al. (2011) U–Pb ages and Hf–O isotopes of zircons from  
903           Late Paleozoic mafic–ultramafic units in the southern Central Asian Orogenic  
904           Belt: Tectonic implications and evidence for an Early-Permian mantle plume.  
905           *Gondwana Research* 20:516-531 doi:10.1016/j.gr.2010.11.015

906   Su B-X, Qin K-Z, Tang D-M, Sakyi PA, Liu P-P, Sun H, Xiao Q-H (2013) Late  
907           Paleozoic mafic–ultramafic intrusions in southern Central Asian Orogenic Belt  
908           (NW China): Insight into magmatic Ni–Cu sulfide mineralization in orogenic  
909           setting.           *Ore           Geol           Rev*           51:57-73  
910           doi:http://dx.doi.org/10.1016/j.oregeorev.2012.11.007

911   Sun H (2009) Ore-forming mechanism in conduit system and ore-bearing property  
912           evaluation for mafic–ultramafic complex in Eastern Tianshan, Xinjiang.

913 Unpublished PhD thesis. Institute of Geology and Geophysics, Chinese  
 914 Academy of Sciences. p274

915 Sun T, Qian Z-Z, Li C, Xia M-Z, Yang S-H (2013a) Petrogenesis and economic  
 916 potential of the Erhongwa mafic–ultramafic intrusion in the Central Asian  
 917 Orogenic Belt, NW China: Constraints from olivine chemistry, U–Pb age and  
 918 Hf isotopes of zircons, and whole-rock Sr–Nd–Pb isotopes. *Lithos* 182-  
 919 183:185-199 doi:10.1016/j.lithos.2013.10.004

920 Sun T, Qian ZZ, Deng YF, Li CS, Song XY, Tang QY (2013b) PGE and Isotope (Hf-  
 921 Sr-Nd-Pb) Constraints on the Origin of the Huangshandong Magmatic Ni-Cu  
 922 Sulfide Deposit in the Central Asian Orogenic Belt, Northwestern China. *Econ*  
 923 *Geol* 108:1849-1864 doi:10.2113/econgeo.108.8.1849

924 Tang D, Qin K, Li C, Qi L, Su B, Qu W (2011) Zircon dating, Hf–Sr–Nd–Os isotopes  
 925 and PGE geochemistry of the Tianyu sulfide-bearing mafic–ultramafic intrusion  
 926 in the Central Asian Orogenic Belt, NW China. *Lithos* 126:84-98  
 927 doi:10.1016/j.lithos.2011.06.007

928 Tang D, Qin K, Su B et al. (2013) Magma source and tectonics of the Xiangshanzhong  
 929 mafic–ultramafic intrusion in the Central Asian Orogenic Belt, NW China,  
 930 traced from geochemical and isotopic signatures. *Lithos* 170–171:144-163  
 931 doi:http://dx.doi.org/10.1016/j.lithos.2013.02.013

932 Taylor JR, Wall VJ, Pownceby MI (1992) The calibration and application of accurate  
 933 redox sensors. *Am Mineral* 77:284-295

- 934 Tian W, Campbell IH, Allen CM et al. (2010) The Tarim picrite-basalt-rhyolite suite, a  
935 Permian flood basalt from northwest China with contrasting rhyolites produced  
936 by fractional crystallization and anatexis. *Contrib Mineral Petr* 160:407-425  
937 doi:DOI 10.1007/s00410-009-0485-3
- 938 Wang RM, Zhao CL (1991) Kalatongke Cu-Ni Sulfide No. 1 Ore Deposit in Xinjiang.  
939 Geological Publishing House, Beijing. 1-319
- 940 Wang RM, Liu DQ, Yin DT (1987) The conditions of controlling metallogny of Cu-Ni  
941 sulfide ore deposits and the orientation of finding ore Hami, Xinjiang, China.  
942 *Journal of Mineralogy and Petrology* 7:1-152
- 943 Wang Y, Zhang Z, You M, Li X, Li K, Wang B (2015) Chronological and gechemical  
944 charcateristics of the Baixintan Ni-Cu deposit in Eastern Tianshan Mountains,  
945 Xinjiang, and their implications for Ni-Cu mineralization. *Geol China* 42:452-  
946 467
- 947 Xia M-Z, Jiang C-Y, Li C, Xia Z-D (2013) Characteristics of a Newly Discovered Ni-  
948 Cu Sulfide Deposit Hosted in the Poyi Ultramafic Intrusion, Tarim Craton, NW  
949 China. *Econ Geol* 108:1865-1878 doi:10.2113/econgeo.108.8.1865
- 950 Xiao WJ, Windley BF, Huang BC et al. (2009) End-Permian to mid-Triassic termination  
951 of the accretionary processes of the southern Altaids: implications for the  
952 geodynamic evolution, Phanerozoic continental growth, and metallogeny of  
953 Central Asia. *Int J Earth Sci (Geol Rundsch)* 98:1189-1217 doi:DOI  
954 10.1007/s00531-008-0407-z

- 955 Xue S, Qin K, Li C, Tang D, Mao Y, Qi L, Ripley EM (2016) Geochronological,  
956 Petrological, and Geochemical Constraints on Ni-Cu Sulfide Mineralization in  
957 the Poyi Ultramafic-Troctolitic Intrusion in the Northeast Rim of the Tarim  
958 Craton, Western China. *Econ Geol* 111:1465-1484  
959 doi:10.2113/econgeo.111.6.1465
- 960 Yang S-H, Zhou M-F, Lightfoot PC, Xu J-F, Wang CY, Jiang C-Y, Qu W-J (2014) Re-  
961 Os isotope and platinum-group element geochemistry of the Pobei Ni-Cu  
962 sulfide-bearing mafic – ultramafic complex in the northeastern part of the Tarim  
963 Craton. *Miner Deposita* 49:381-397 doi:10.1007/s00126-013-0496-x
- 964 Yang E (2015) Sediment environment and enrichment rule of ore-forming elements of  
965 Lower Cambrian black shale Series, Kuruktag-Beishan region, Xinjiang  
966 Province. PhD thesis. China University of Geosciences, Wuhan, p 150
- 967 Zhang M, Li C, Fu P, Hu P, Ripley E (2011) The Permian Huangshanxi Cu–Ni deposit  
968 in western China: intrusive–extrusive association, ore genesis, and exploration  
969 implications. *Miner Deposita* 46:153-170 doi:10.1007/s00126-010-0318-3
- 970 Zhang ZC, Mao JW, Chai FM, Yan SH, Chen BL, Pirajno F (2009) Geochemistry of  
971 the Permian Kalatongke Mafic Intrusions, Northern Xinjiang, Northwest China:  
972 Implications for the Genesis of Magmatic Ni-Cu Sulfide Deposits. *Econ Geol*  
973 104:185-203
- 974 Zhao Y, Xue C, Zhao X, Yang Y, Ke J (2015) Magmatic Cu–Ni sulfide mineralization  
975 of the Huangshannan mafic–ultramafic intrusion, Eastern Tianshan, China. *J*

976 Asian Earth Sci 105:155-172  
 977 doi:<http://dx.doi.org/10.1016/j.jseaes.2015.03.031>  
 978 Zhao Y, Xue C, Zhao X, Yang Y, Ke J, Zu B (2016) Variable mineralization processes  
 979 during the formation of the Permian Hulu Ni-Cu sulfide deposit, Xinjiang,  
 980 Northwestern China. J Asian Earth Sci 126:1-13  
 981 doi:<http://dx.doi.org/10.1016/j.jseaes.2016.04.021>  
 982 Zhou MF, Leshner CM, Yang ZX, Li JW, Sun M (2004) Geochemistry and petrogenesis  
 983 of 270 Ma Ni-Cu-(PGE) sulfide-bearing mafic intrusions in the Huangshan  
 984 district, Eastern Xinjiang, Northwest China: implications for the tectonic  
 985 evolution of the Central Asian orogenic belt. Chem Geol 209:233-257 doi:DOI  
 986 10.1016/j.chemgeo.2004.05.005



## Figures

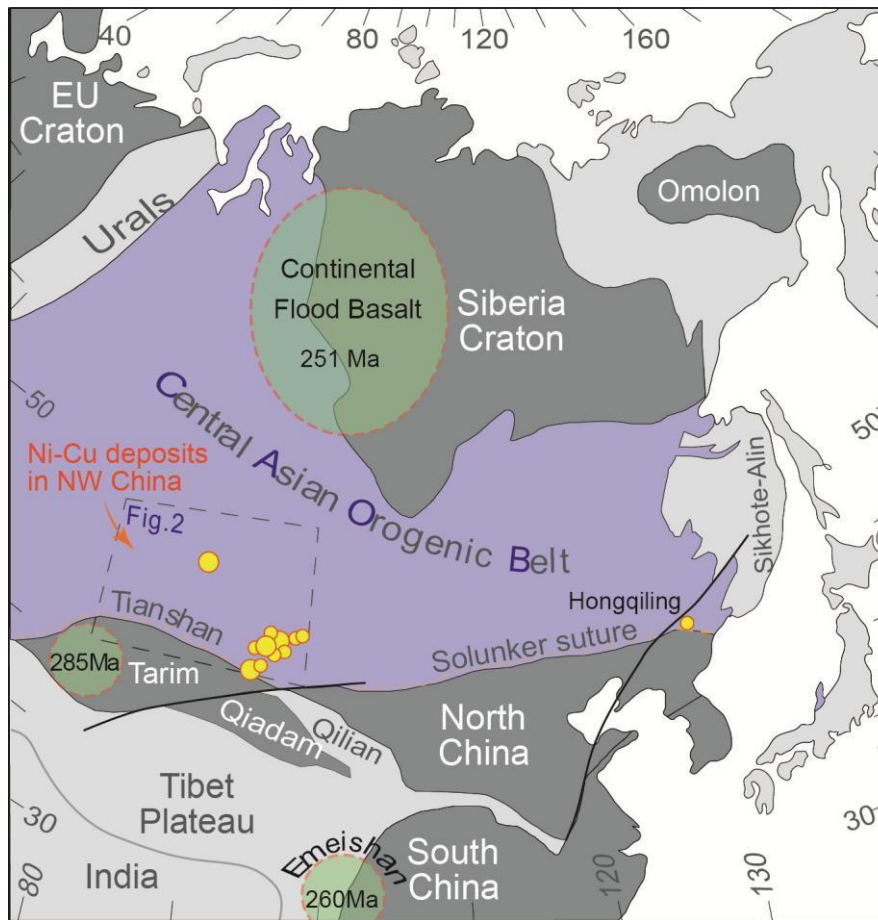


Fig. 1 Spatial distribution of magmatic Ni–Cu deposits in the CAO (modified after Jahn, 2004, Li et al., 2012). Large circle represents Ni–Cu deposits contain Ni metal higher than 0.2 Mt, small circle represents Ni–Cu deposits contain less than 0.2 Mt Ni metal.

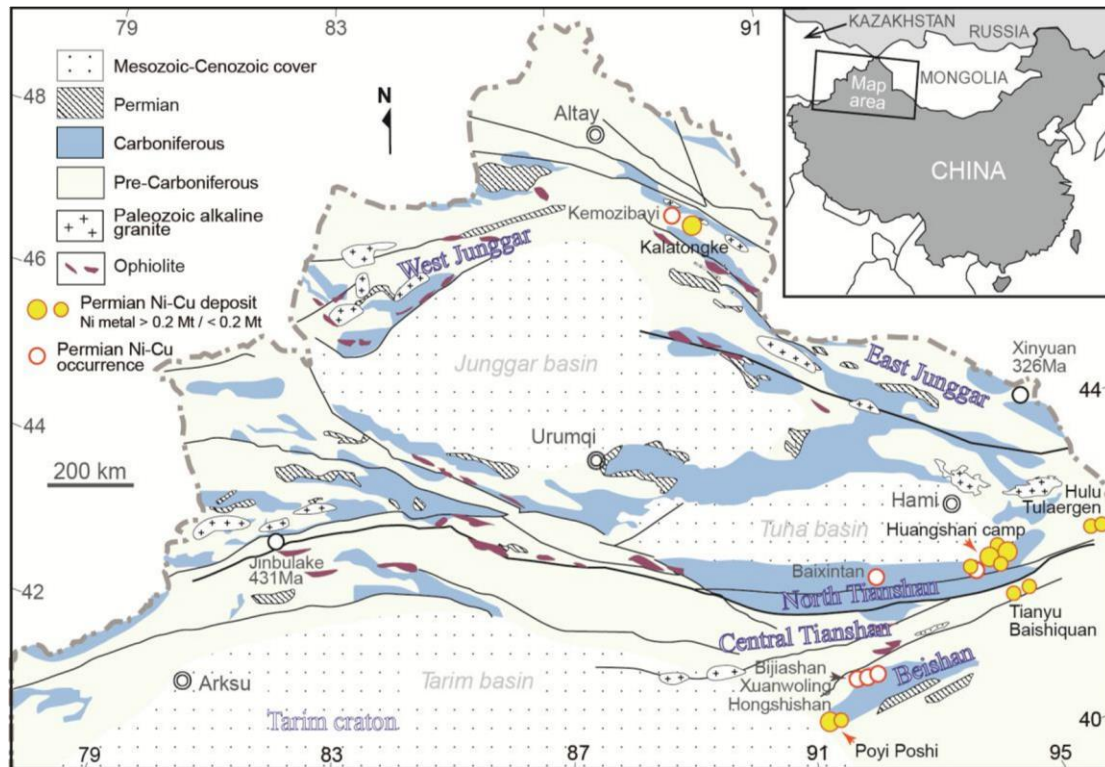


Fig. 2 A simplified geological map of the Xinjiang Uygur Autonomous region in NW China, showing the locality of the Permian mafic-ultramafic deposits/occurrences (modified from Mao et al., 2008). Magmatic Ni-Cu deposits within the Huangshan camp are composed of the Huangshanxi and Huangshandong deposits ( $> 0.2$  Mt Ni metal), the Huangshannan, Xiangshanzhong, and Tudun deposits ( $< 0.2$  Mt Ni metal), and the Erhongwa occurrence.

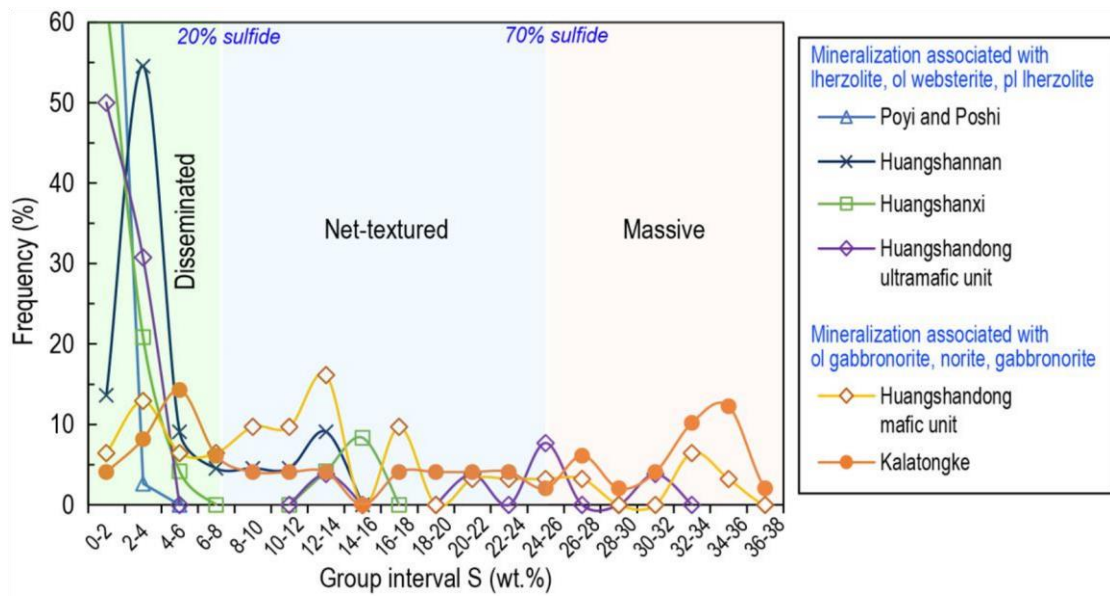


Fig. 3 Frequency distribution of S abundance in ores from the Ni-Cu deposits in the CAOB, illustrating the dominant sulfide texture for these deposits. Data source is listed in Table 1.

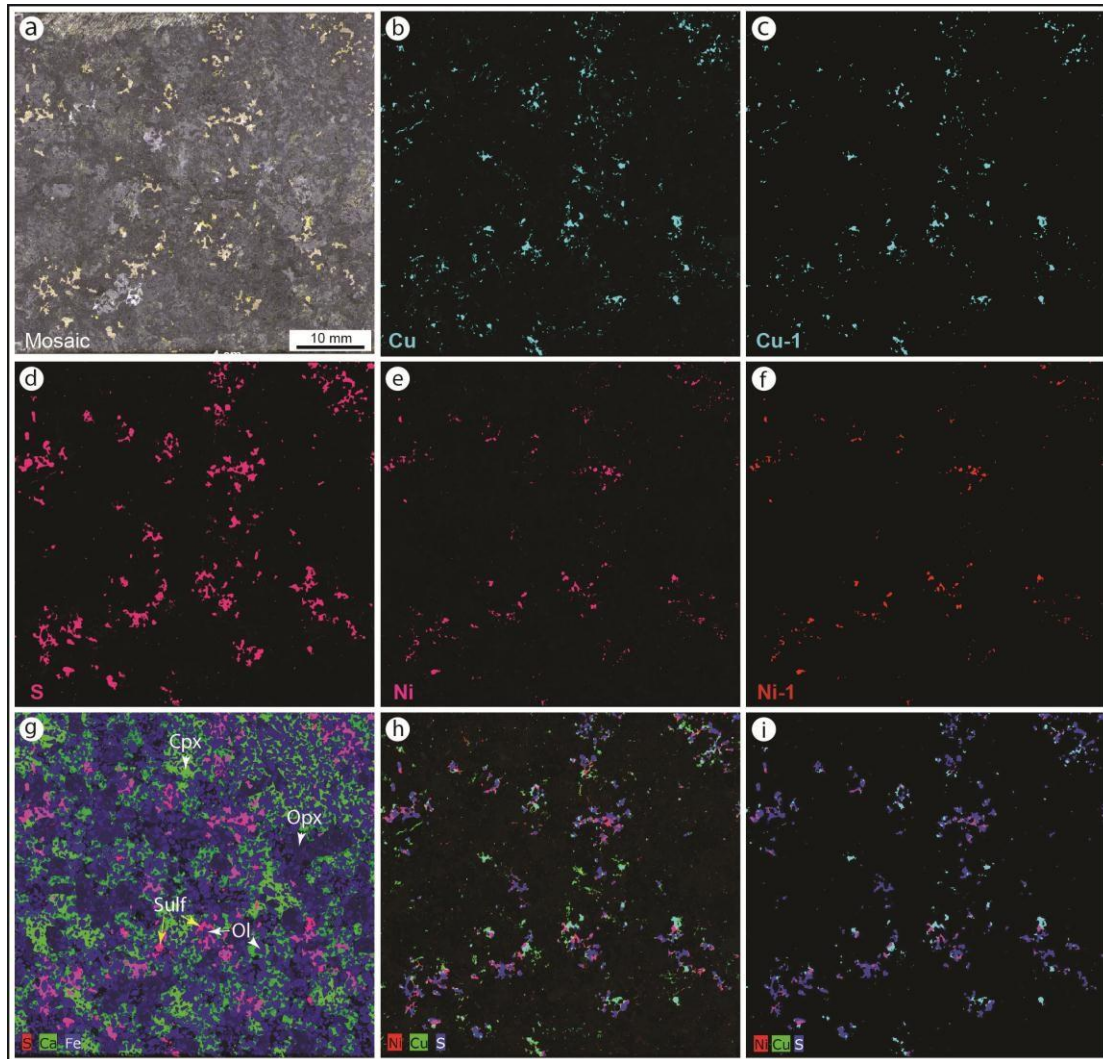


Fig. 4 Optical (a) and XRF images (b–i) of a disseminated lherzolite (06–04–711.5) from the Huangshanxi Ni–Cu deposit. (b), (d), and (e) are raw XRF images of Cu, S, and Ni from Tornado, whereas (c) and (f) are Cu and Ni images after processing; (g) is the combination of S in red, Ca in green, and Fe in blue images showing the distribution of sulfide, olivine, clinopyroxene, and orthopyroxene; (h) and (i) compare the raw XRF three element map (Ni–Cu–S) with the processed map.

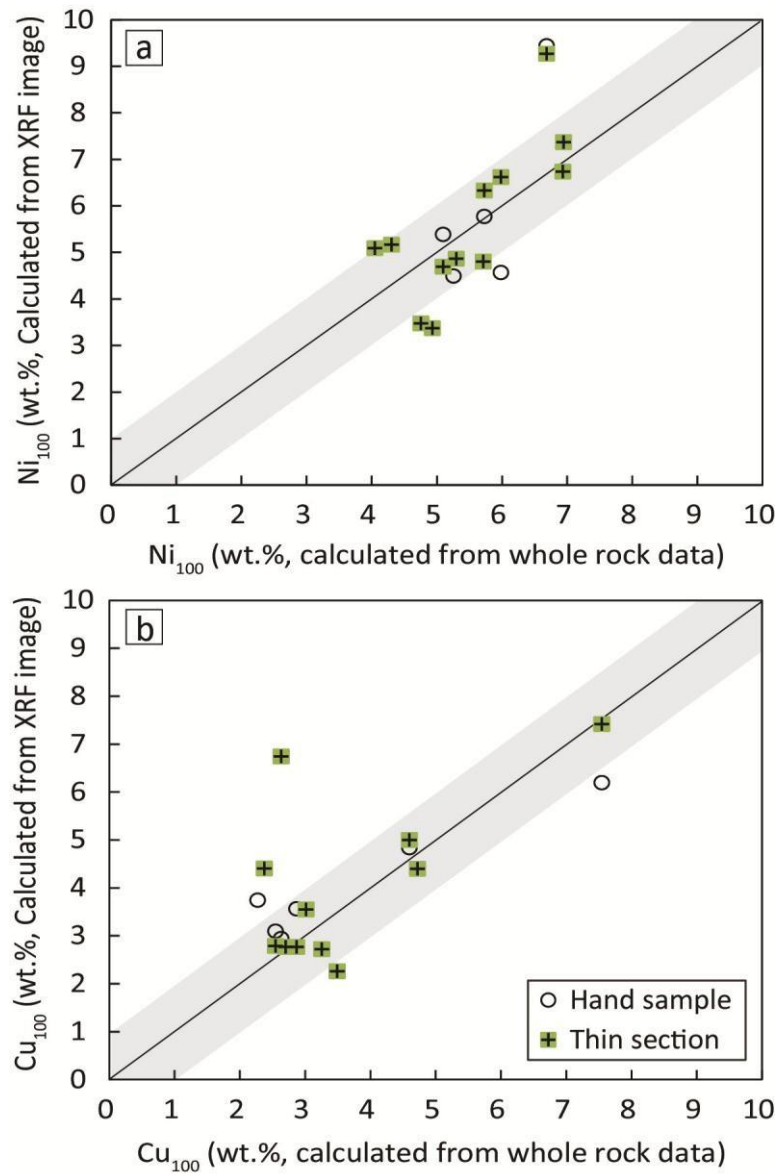
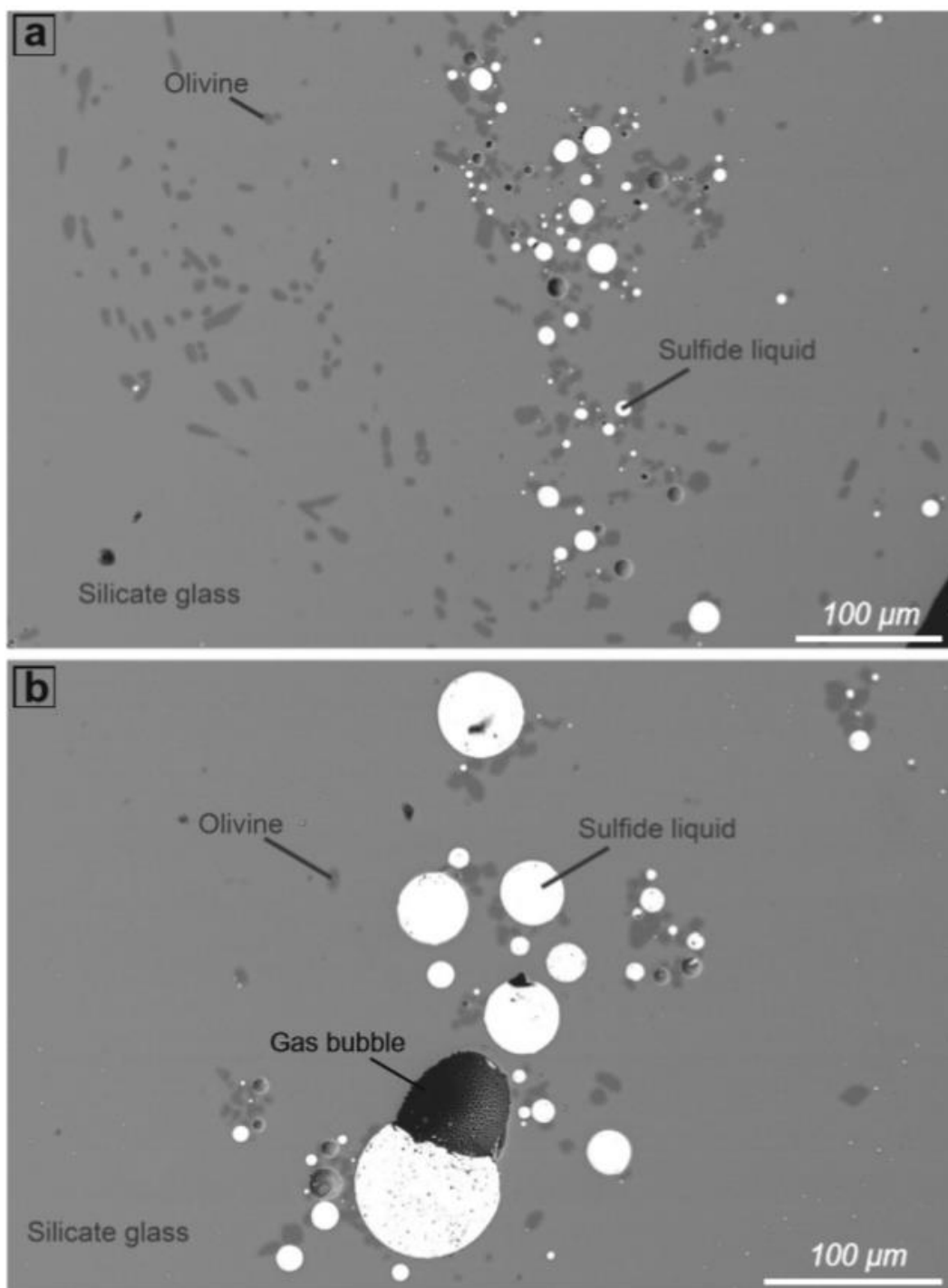


Fig. 5 Comparison between Ni tenors (a) and Cu tenors (b) calculated using whole rock S, Cu, Ni contents and these estimated by XRF images at both hand sample scale and thin section scale. Mineralized samples from the Huangshanxi (Mao et al., 2014) and Tudun (this study) Ni–Cu deposits are used for comparison.



1025

1026 Fig. 6 Back-scattered electron images of a typical experimental product (sample  
 1027 GV159), showing the coexistence of silicate glass, sulfide droplets (with sensibly  
 1028 different sizes in a and b), olivine, and gas bubbles (b).



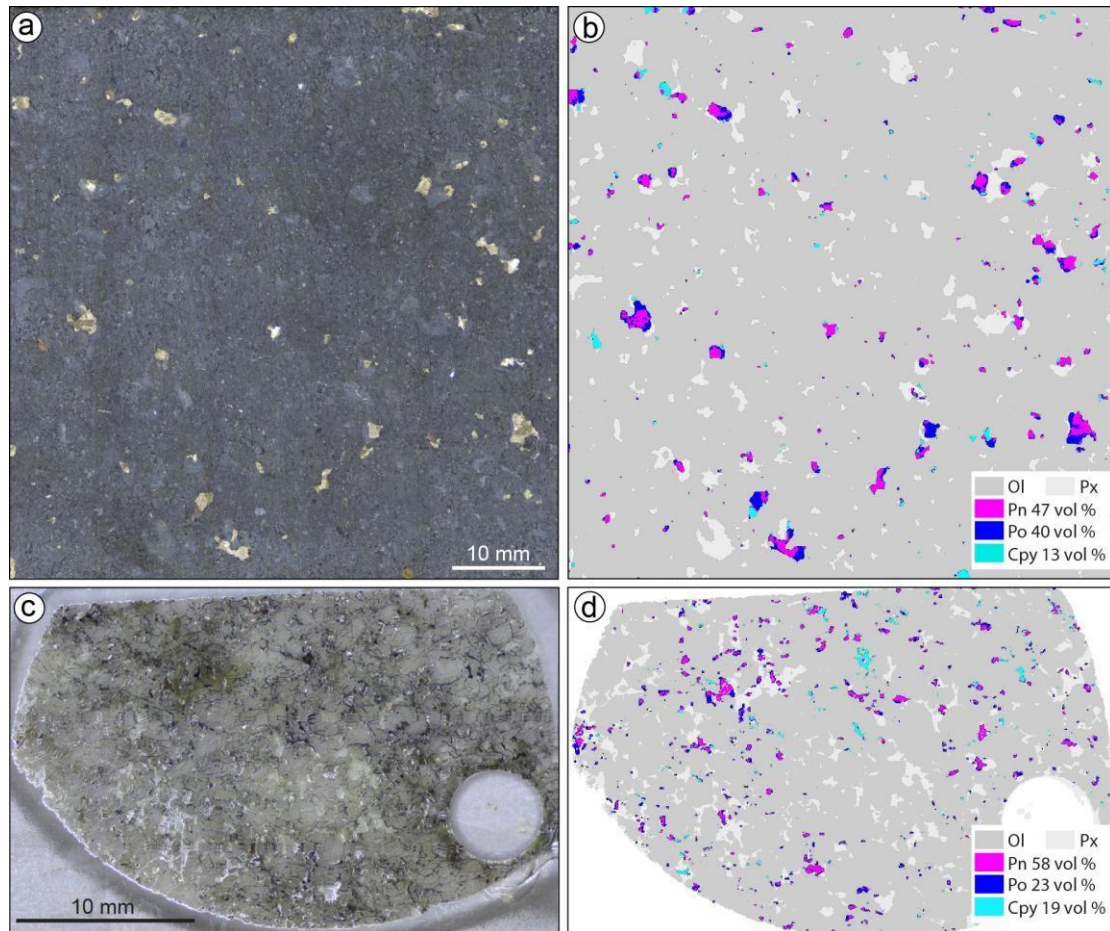


Fig. 8 Optical (a, c) and XRF image (b, d) of lherzolite from the Poyi deposit. The XRF image is shown as false-color showing the proportion of pentlandite, chalcopyrite, and pyrrhotite in 100% sulfide.

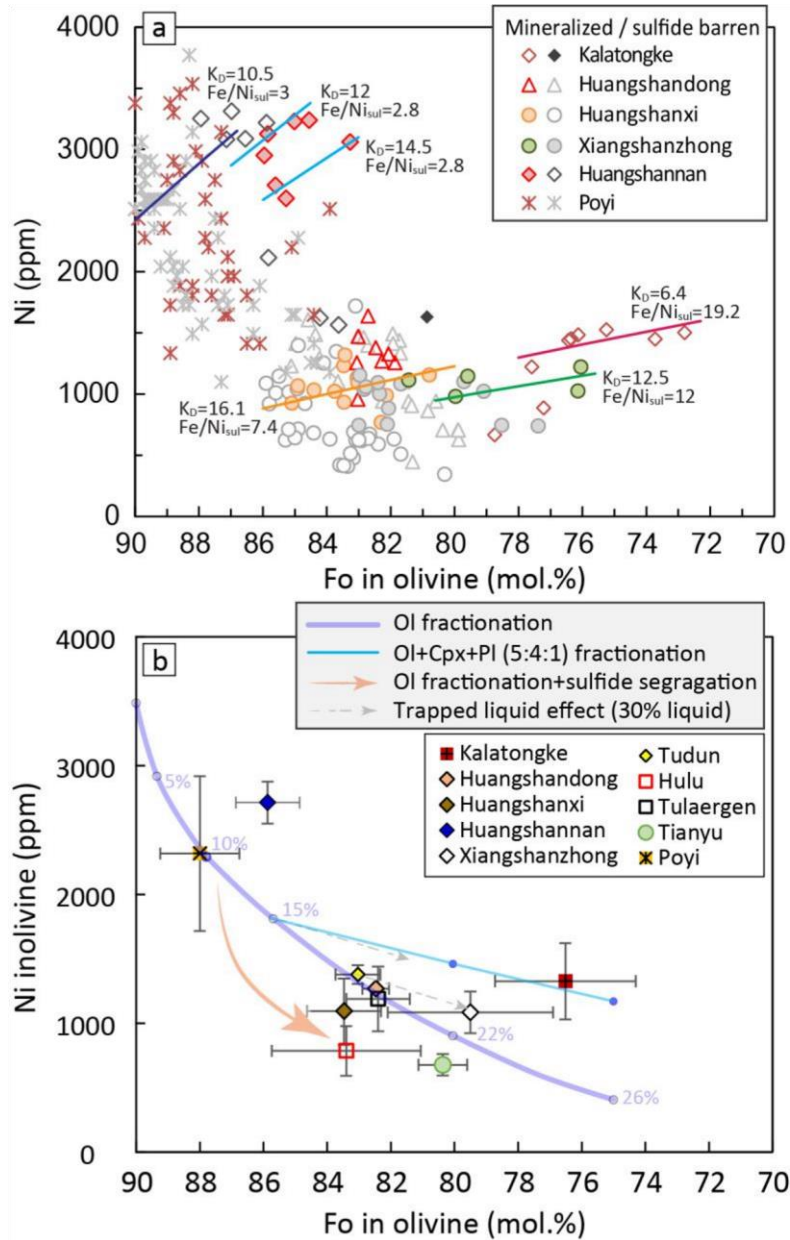


Fig. 9 Olivine compositional variation in Ni–Cu deposits in NW China. a Olivine compositional variation in samples from the Kalatongke, Huangshandong, Huangshanxi, Xiangshanzhong, Huangshannan, and Poyi deposits, illustrating negative correlations between Ni and Fo value which are derived from Fe/Ni exchange between olivine and sulfide. KD and Fe/Ni ratio in sulfide (Fe/Ni<sub>sul</sub>) are listed in Tables 4 and 5. Other deposits are not plotted for clarity. b Average olivine composition for each deposit. Error bars are 2σ uncertainty. Data sources are listed in Table 1 and the parameters used in the model calculation are listed in Table 7. See text for the detailed explanation of the modeling lines.



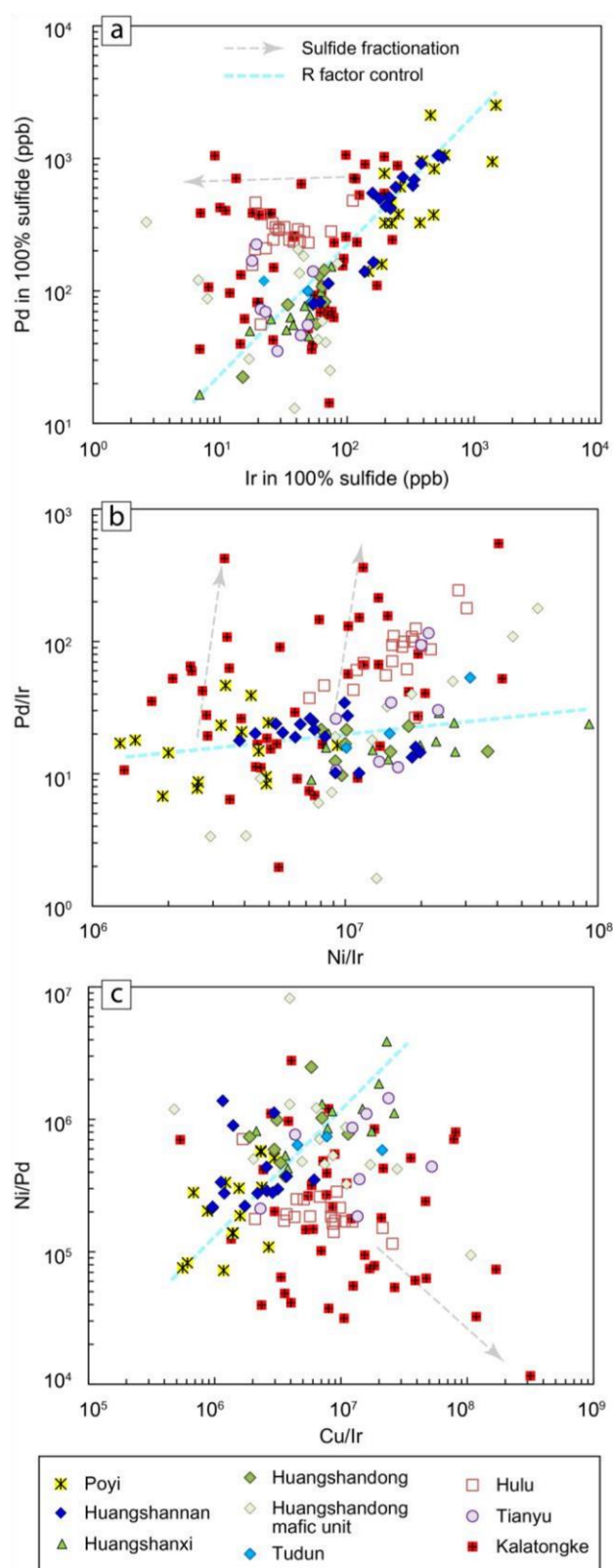


Fig. 5 Plots of Ir and Pd tenors (a) and Pd/Ir vs Ni/Ir ratios (b) and Ni/Pd vs Cu/Ir ratios (c) in sulfide from the Ni–Cu deposits in NW China.

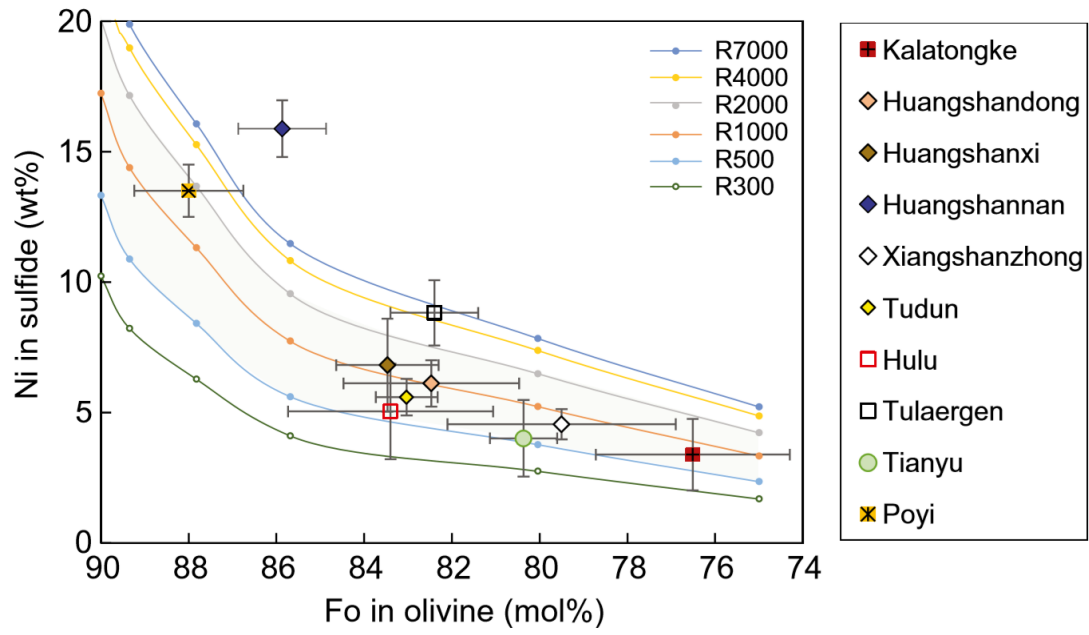


Fig.10 Correlation between Fo value in olivine and Ni in sulfide of the Ni-Cu deposits in NW China. Error bars are  $2\sigma$  uncertainty. The parameters used in the R value calculation are listed in Table 7. See text for the detailed explanation of the modeling lines.

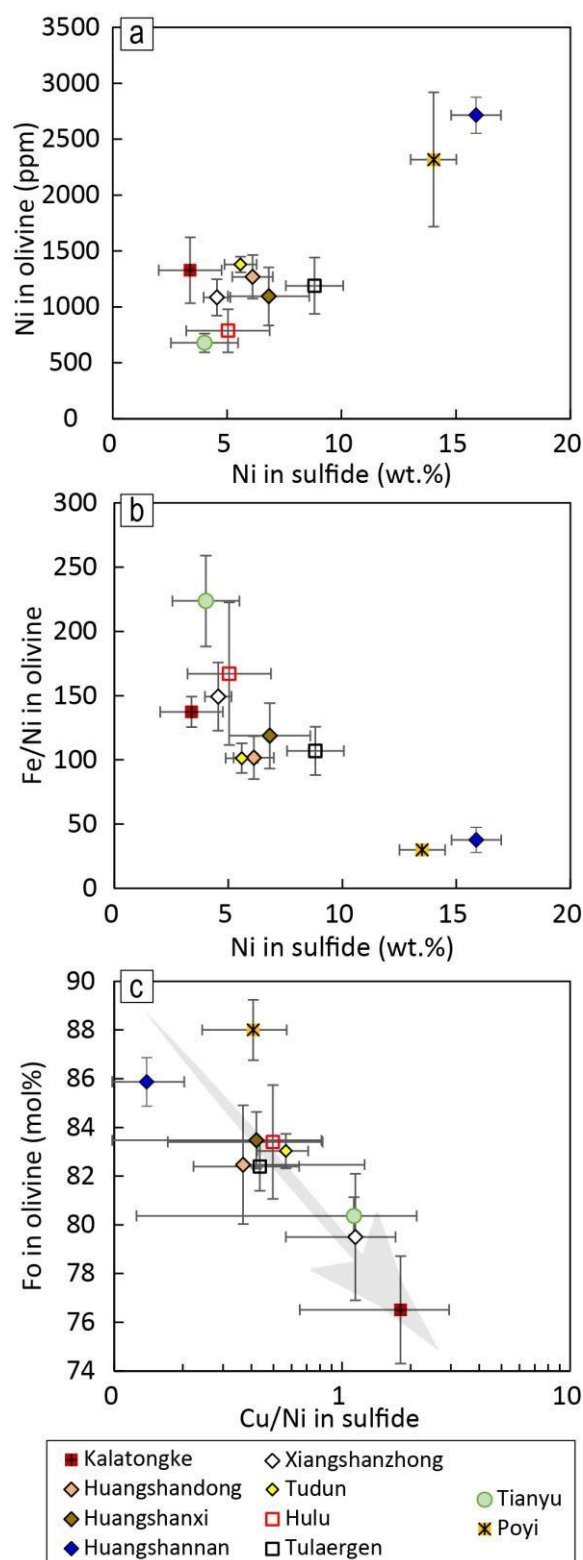
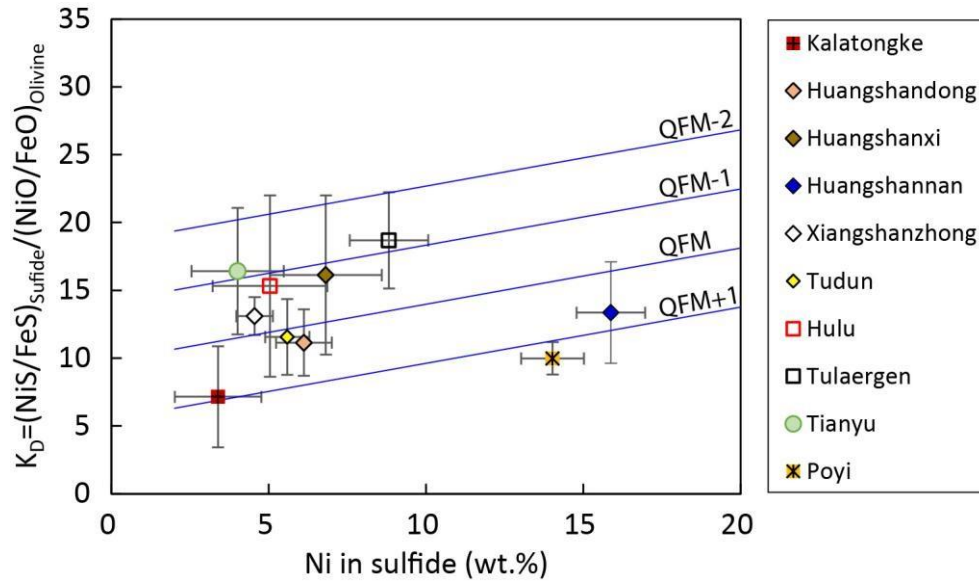


Fig. 11 Plots of Ni tenor in sulfide versus Ni content (a) and Fe/Ni ratio (b) in olivine, correlation between Cu/Ni ratios in sulfide and Fo values in olivine. Gray arrows illustrate that the Ni tenor in sulfide increases with the increase of Ni content in olivine (a) and with the decrease of Fe/Ni ratio in olivine (b), and Cu/Ni ratio in sulfide increases as Fo value in olivine decreases (c) for the Ni-Cu deposits in NW China. Error bars are  $2\sigma$  uncertainty

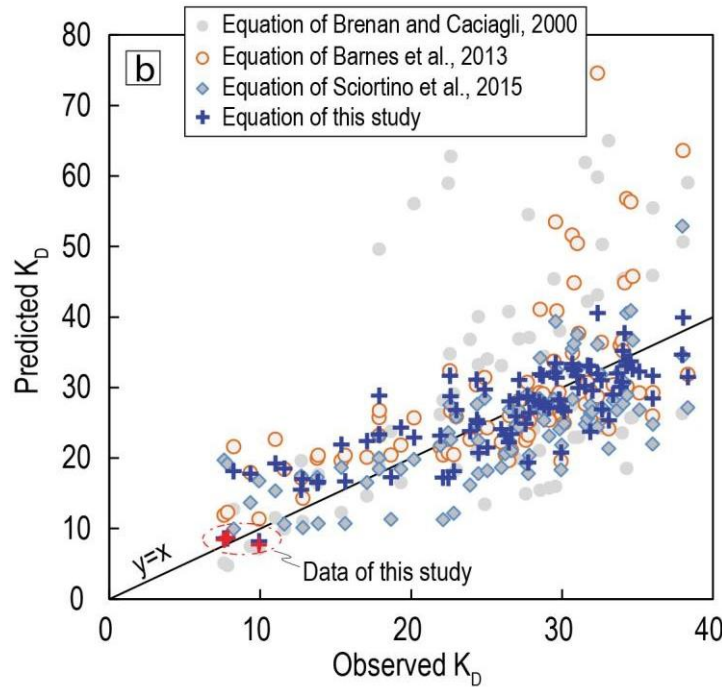
1062



1063

1064 Fig. 12 Ni tenor in sulfide versus KD values. The baselines of oxygen fugacity were  
 1065 calculated using the recalibrated equation of this study. Error bars of the Tianyu and  
 1066 Hulu deposits are  $2\sigma$  uncertainty. The error of KD in the individual sample is  
 1067 approximately  $\pm 3.5$

1068

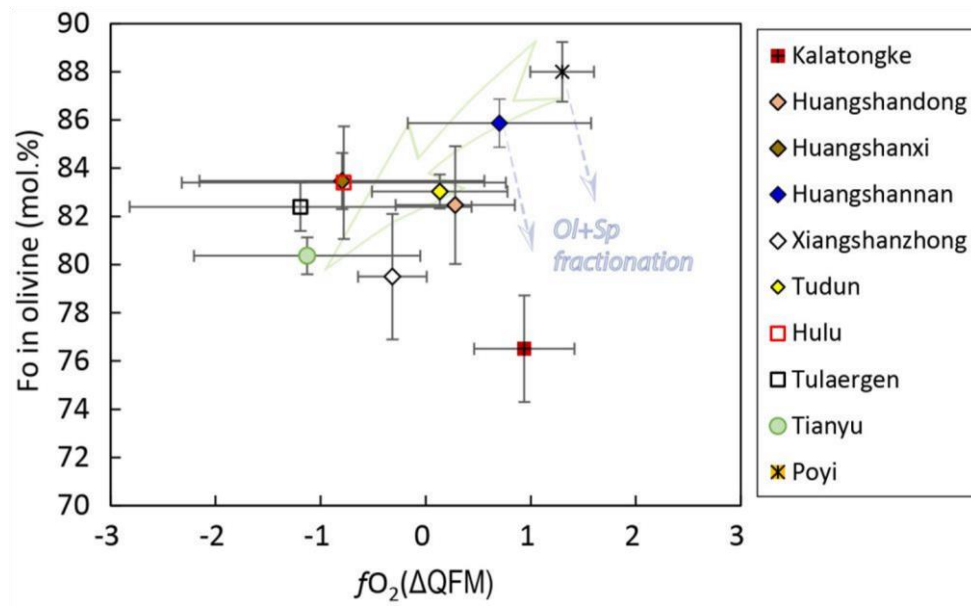


1069

1070

1071 Fig. 13 Comparison of predicted KD and observed KD estimated by different  
 1072 equations. See Fig. 7 for the data source

1073



1074

1075 Fig. 14 Plot of oxygen fugacity shown as  $\Delta QFM$  versus Fo values in olivine for the Ni–  
 1076 Cu deposits in NW China. The green arrows show that the oxidation state of the Ni–Cu  
 1077 deposits in the East Tianshan is becoming increasingly reduced as Fo value in olivine  
 1078 decreases; blue dashed lines illustrate the oxidation state of the Poyi and  
 1079 Huangshannan host magmas which slightly increases during olivine and spinel  
 1080 fractionation. Error bars of the Tianyu and Hulu deposits are  $2\sigma$  uncertainty. The error  
 1081 of  $\Delta QFM$  in the individual sample is approximately  $\pm 0.8$  log unit of  $\Delta QFM$   
 1082

1083

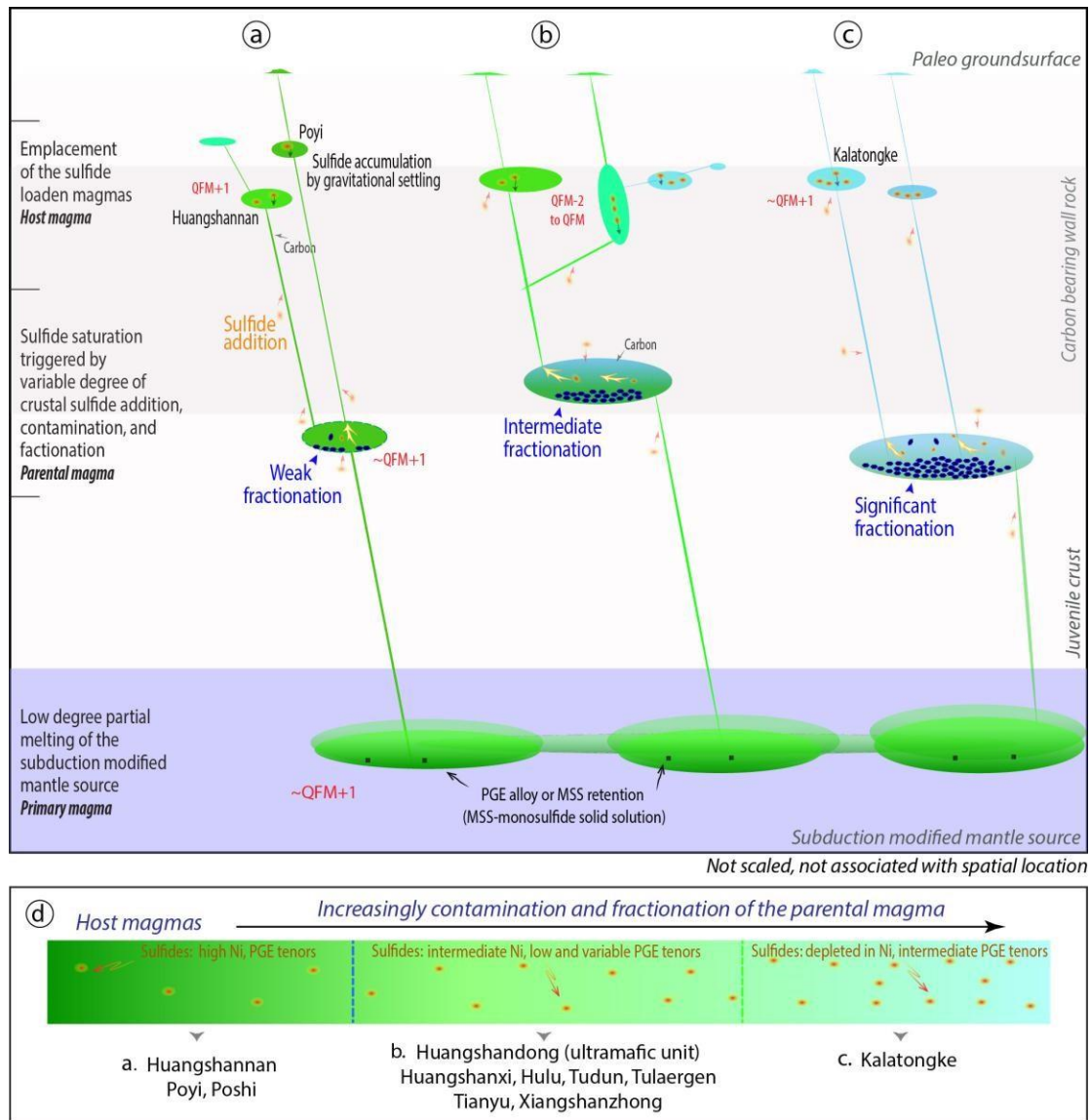


Fig. 15 A genetic model for the Ni–Cu deposits in NW China, showing the evolution of the Permian mantle partial melts in the continental crust (a-d). The relatively low degree of partial melting generated relatively oxidizing primary magma with substantial Ni and Cu but low PGE concentrations, leaving PGE alloy or sulfide in the mantle residue (a-c). Weak to significant fractionation and contamination by sulfide and reducing agents in the staging chamber or during ascent gave rise to magmas with variable oxygen fugacity (a-c) and Ni and Cu contents(d), whereas PGE concentrations were not significantly modified during magma evolution

1097 **Table captions**

1098 Table 1. Compiled features of the Permian Ni–Cu deposits (occurrences) in the Central

1099 Asian Orogenic Belt.

Location	Deposit	Zircon Age (r), Ma	Host rock of Zircon	Surface area (km <sup>2</sup> )	Intrusion shape	Rock types associated with mineralization	Sulfide texture	Country rocks	Xenolith	Graphite bearing wall rocks in the region	Reserves (Mt) @ Ni, Cu grades (wt.%)	References
North Tianshan	Huangshanxi	284 (3)	Gabbro	1.71	Satellite, elongate rhomb	Lherzolite, ol websterite	Disseminated	Lower Carboniferous Gandun group	Carbon-bearing slate	Abundant of carbon-bearing slates	65@0.49 Ni, 0.3 Cu	Wang et al., 1987; Mao et al., 2008; Qin et al., 2011
North Tianshan	Huangshandong	274 (3)	Ol norite	2.8	Elongate rhomb	Lherzolite, ol websterite, ol gabbro, ol websterite, ol gabbro	Disseminated, densely disseminated	Lower Carboniferous Gandun group	Carbon-bearing slate	Abundant of carbon-bearing slates	69@0.52 Ni, 0.27 Cu	Wang et al., 1987; Mao et al., 2008; Qin et al., 2011
North Tianshan	Huangshannan	278 (2)	Ol gabbro	4.22	Elongate rhomb	Lherzolite, ol websterite	Disseminated	Lower Carboniferous Gandun group	Carbon-bearing slate	Abundant of carbon-bearing slates	30@0.4Ni, 0.1Cu	Wang et al., 1987; Mao et al., 2016
North Tianshan	Xiangshanzhong	279.6 (1.1)	Gabbro	2.8	Dike like	Pl lherzolite, pl ol websterite, gabbro	Disseminated	Lower Carboniferous Wutongwozi group	Unknown	Abundant of carbon-bearing slates	8@0.5Ni, 0.3Cu	Wang et al., 1987; Mao et al., 2008; Han et al., 2010
North Tianshan	Tudun	280 (3)	Gabbro	0.98	Chondolite	Pl lherzolite, gabbro	Disseminated	Lower Carboniferous Gandun group	Unknown	Abundant of carbon-bearing slates	5@0.3Ni, 0.2Cu	Wang et al., 1987; Mao et al., 2008; Qin et al., 2011
North Tianshan	Hulu	282.3 (1.2)	Gabbro	0.75	Chondolite	Lherzolite, ol websterite	Disseminated	Lower Carboniferous Wutongwozi group	Unknown	Abundant of carbon-bearing slates	18@0.44Ni, 0.37Cu	Sun 2009; Han et al., 2013
North Tianshan	Tulaergen	~280**	Pl lherzolite	0.005	Dike like	Pl lherzolite, pl ol websterite	Dense disseminated, net-textured	Upper Carboniferous volcanic rocks	Gabbro, tuff	Minor carbon-bearing slates	24@0.42Ni, 0.27Cu	Mao et al., 2008; Sun, 2009; Qin et al., 2011; unpublished data
North Tianshan	Baixintan*	278 (2)	Pl lherzolite	2.1	Chondolite	Pl ol websterite	Disseminated	Ordovician volcanic rocks	Unknown	Unknown	/	Li et al., 2014; Wang et al., 2015
North Tianshan	Erhongwa*	283 (2)	Olivine gabbro	6.25	Elliptical	Pl lherzolite	Weakly disseminated	Lower Carboniferous Gandun group	Unknown	Abundant of carbon-bearing slates	/	Wang et al., 1987; Sun et al., 2013a
Central Tianshan	Tianyu	280 (2)	Gabbro	0.0056	Dike like	Lherzolite, ol websterite	Disseminated	Precambrian schist, gneiss	Granite	Absent of carbon-bearing slates, minor black shales	Unknown	Wang et al., 1987; Mao et al., 2008; Qin et al., 2011
Central Tianshan	Baishiquan	284.8 (5.7)	Gabbro	~2	Chondolite plus dike	Pl lherzolite, gabbro	Disseminated, net-textured	Precambrian schist, gneiss	Gneiss	Absent of carbon-bearing slates, minor black shales	29@0.32Ni, 0.24Cu	Wang et al., 1987; Mao et al., 2008; Qin et al., 2011; Su et al., 2010
Beishan	Poyi	269.9 (1.7)	Troctolite	1***	Chondolite	Dunite, wehrlite	Disseminated	Lower Carboniferous Hongliuhe group, Precambrian schist and gneiss	Marble, minor gabbro	Minor carbon-bearing slates	67@0.3Ni	Xue et al., 2016
Beishan	Poshi	284 (2.2)	Olivine gabbro	0.6***	Elliptical	Dunite, wehrlite	Disseminated	Lower Carboniferous Hongliuhe group, Precambrian schist and gneiss	Marble, minor gabbro	Minor carbon-bearing slates	/	Qin et al., 2011
Beishan	Hongshishan*	286.4 (2.8)	Troctolite	6.8	Chondolite	Dunite, wehrlite, lherzolite	Weakly disseminated	Lower Carboniferous Hongliuhe group	Unknown	Minor carbon-bearing slates	/	Su et al., 2011
Beishan	Luodong*	284 (2.3)	Gabbro	1.5	Rhomb	Dunite, wehrlite, lherzolite	Weakly disseminated	Precambrian schist	Unknown	Minor carbon-bearing slates	/	Su et al., 2011
Beishan	Xuanwoing*	260.7 (2)	Gabbro	7.4	Chondolite	Dunite, wehrlite, lherzolite	Weakly disseminated	Lower Carboniferous Hongliuhe group	Unknown	Minor carbon-bearing slates	/	Su et al., 2011
Beishan	Bijashan*	279 (2)	Gabbro	0.7***	Elliptical	Dunite, wehrlite, lherzolite	Weakly disseminated	Lower Carboniferous Hongliuhe group	Unknown	Minor carbon-bearing slates	/	Qin et al., 2011
East Junggar	Kemozabay*	~280**	Pl ol websterite	<1	Unclear	Pl lherzolite, pl ol websterite	Disseminated	Carboniferous Nanmingshui Formation	Unknown	Abundant of carbon-bearing slates	/	Tang et al., under review
East Junggar	Kalatongke	287 (5)	Norite	0.05	Weakly elongate rhomb, funnel shape	Ol gabbro, ol websterite	Net-textured, Massive ore	Carboniferous Nanmingshui Formation	Tuff, slate	Abundant of carbon-bearing slates	38@0.70Ni, 1.19Cu	Han et al., 2004; Annual resource report of 2011 published by the mining company

\*occurrences, some of these intrusions are still in exploration, \*\*unpublished data, \*\*\*area for ultramafic units

1100

1101

1102 Table 2. Summary and results of experiments of Fe–Ni exchange between olivine and

1103 sulfide.

Table 2. Summary and results of experiments of Fe-Ni exchange between olivine and sulfide.

Experiment ID	Duration (h)	T (°C)	P (MPa)	log $fO_2$	$\Delta FMQ$	log $fS_2^*$			
GV52	3	1200	64.6	-7.85	0.4	0.88			
GV115Palu	1	1200	67.7	-7.72	0.53	1.03			
GV115P	1	1200	67.7	-7.95	0.3	0.77			
GV128	1	1200	71.9	-9.03	-0.78	-0.59			
GB91	1	1200	81.2	-7.58	0.66	1.12			
GV159	1	1200	76.5	-6.13	2.11	2.86			
GV160	1	1200	77.8	-6.97	1.27	1.87			
<i>Olivine composition</i>									
Experiment ID	$n$	SiO <sub>2</sub>	MgO	FeO	NiO	CaO	Total	Fo	
GV52	41	40.61	50.78	10.21	0.04	0.43	101.6	89.9	
	$\sigma$	0.21	0.69	0.6	0.03	0.19			
GV115Palu	40	40.76	50.47	9.7	0.04	0.43	101.7	90.3	
	$\sigma$	0.22	0.4	0.3	0.02	0.14			
GV115P	32	40.68	50.07	10.18	0.03	0.43	101.7	89.8	
	$\sigma$	0.25	0.51	0.39	0.01	0.19			
GV128	31	40.25	46.96	13.56	0.02	0.35	101.2	86.2	
	$\sigma$	0.36	1.1	1.29	0.01	0.06			
GB91	50	40.85	49.25	10.74	0.05	0.3	101.3	89.2	
	$\sigma$	0.25	0.49	0.28	0.02	0.07			
GV159	8	41.19	49.66	9.88	0.13	0.46	101.3	90.0	
	$\sigma$	0.16	0.41	0.27	0.07	0.19			
GV160	8	41.12	49.05	10.43	0.19	0.34	101.1	89.4	
	$\sigma$	0.24	0.43	0.59	0.05	0.1			
<i>Sulfide composition</i>									
Experiment ID	$n$	Fe	Ni	Cu	S	O	Total		
GV52	62	54.9	1.8	1.9	36.5	2.4	97.8		
	$\sigma$	0.8	0.4	0.4	0.6	0.2			
GV115Palu	35	55.4	1.7	2.6	35.9	2.4	98.2		
	$\sigma$	0.5	0.2	0.2	0.7	0.2			
GV115P	49	56	1.6	1.8	36.2	2.5	98.1		
	$\sigma$	0.6	0.2	0.3	0.5	0.2			
GV128	48	59.2	0.8	0.9	33.2	4	98.3		
	$\sigma$	0.8	0.3	0.2	0.6	0.5			
GB91	34	53.9	2.2	4.1	36.3	2.8	99.4		
	$\sigma$	0.9	0.4	0.9	0.5	0.4			
GV159	13	55	2.1	2.9	36.4	2.8	99.4		
	$\sigma$	0.7	0.3	0.4	0.3	0.5			
GV160	10	43.8	7	8.1	35.4	1.9	99.6		
	$\sigma$	2.8	1.3	2.5	0.8	0.3			

\* $fS_2$  is calculated from the equation of Mungall and Brenan, 2014;  $n$  is the number of analyses



1105 Table 3. Compositions of pentlandite, pyrrhotite, and chalcopyrite from the Kalatongke,  
 1106 Huangshanxi, Huangshannan, Xiangshanzhong, Tudun, and Poyi deposits.

Sample	Deposit	<i>n</i>	S	Fe	Co	Ni	Fe/Ni	Total	Co/Ni
Y1-700-25-8	Kalatongke	5	33.2	28.4	1.3	35.8	1.26	98.8	26.9
Y2-528-3-8	Kalatongke	5	33.3	29.0	1.4	35.5	1.22	99.2	25.4
Y2-350-31-2	Kalatongke	5	33.2	30.2	1.4	35.1	1.16	100.0	25.6
Y1-650-30-4	Kalatongke	5	32.9	28.4	1.3	35.6	1.25	98.3	26.8
06-18-919	Huangshanxi	6	32.9	30.3	1.6	34.1	1.13	98.9	20.8
06-04-626.7	Huangshanxi	6	32.8	30.7	1.7	33.3	1.08	98.5	19.4
06-04-651	Huangshanxi	6	33.3	29.9	1.5	34.2	1.14	98.9	22.4
06-04-672.6	Huangshanxi	6	33.4	29.1	1.8	34.3	1.18	98.7	18.8
06-04-711.5	Huangshanxi	6	33.2	29.4	2.0	34.0	1.16	98.6	17.3
06-18-944..3	Huangshanxi	6	33.1	29.5	1.8	34.2	1.16	98.4	19.3
HSN455	Huangshannan	5	33.1	31.9	0.6	33.4	1.05	99.0	59.6
14HSN36	Huangshannan	5	33.0	30.9	0.6	34.0	1.10	98.5	53.0
15-4-7	Huangshannan	5	33.0	30.3	0.7	34.5	1.14	98.6	46.7
ZK3693-279	Xiangshanzhong	7	33.2	32.0	1.7	32.1	1.00	99.0	18.9
ZK3693-296	Xiangshanzhong	5	33.3	31.7	2.1	32.7	1.03	99.8	15.8
ZK3693-308	Xiangshanzhong	5	33.5	31.5	1.8	33.0	1.05	99.8	18.3
ZK36953-341	Xiangshanzhong	5	32.9	31.8	1.8	32.0	1.01	98.5	17.8
TD545-4	Tudun	5	33.2	28.8	1.7	36.1	1.25	99.8	21.2
TD505-2	Tudun	5	33.2	28.0	1.5	37.0	1.32	99.6	24.6
TD545-1	Tudun	5	33.1	28.7	1.8	36.3	1.26	99.9	20.1
ZK11-1-197.5	Tudun	5	33.0	28.4	2.1	36.0	1.27	99.5	17.1
ZK11-1-206.5	Tudun	5	33.2	28.3	2.4	35.5	1.26	99.4	14.8
PYZK23-3-761	Poyi	9	33.3	37.4	0.9	27.3	0.73	98.8	31.7
PYZK23-3-1057	Poyi	6	32.7	32.6	0.7	32.5	1.00	98.5	46.5
PYZK23-3-948	Poyi	5	32.4	33.0	0.7	32.0	0.97	98.1	43.2
<i>n-number of analysis</i>									

1107

1108

1109

1110

1111

1112 Table 4. Compositions of sulfide and olivine of the Kalatongke, Huangshanxi,

1113 Huangshannan, Xiangshanzhong, Tudun, and Poyi deposits.

Sample	Rock type	Scale	Deposit	S*	Pn	Cpy	Po	Ni	Cu	Fe	S	Ni/Cu	Fe/Ni sulfide	Fe/Ni olivine	Ni olivine	Fe/Ni olivine	KD
				wt.%	vol.%	vol.%	vol.%	wt.%	wt.%	wt.%	wt.%		mol.%	mol.%	ppm	mol.%	
Y1-700-25-8	Ol gabbronorite	Thin section	Kalatongke	1.9	15	19	66	5.6	5.9	50.5	37.3	0.9	9.4	76.7	1728.0	103.0	10.9
Y2-528-3-8	Ol gabbronorite	Thin section	Kalatongke	20.1	4	35	61	1.3	11.4	49.6	37.4	0.1	/	74.7	1313.1	140.6	/
Y2-528-3-1	Ol gabbronorite	Thin section	Kalatongke	10.1	8	9	83	3.0	2.7	55.9	38.1	1.1	19.6	74.8	1214.6	149.2	7.6
Y2-350-31-2	Ol gabbronorite	Thin section	Kalatongke	7.7	9	22	70	3.5	6.8	52.0	37.6	0.5	15.6	76.3	1514.8	114.4	7.3
Y1-650-30-4	Ol gabbronorite	Thin section	Kalatongke	13.2	7	12	80	3.5	3.9	55.0	38.0	0.9	16.5	72.5	1375.6	142.7	8.6
06-04-626.7	Lherzolite	Hand sample	Huangshanxi	3.1	16	11	72	5.8	3.6	52.3	37.5	1.6	9.5	85.9	1088.0	101.7	10.7
06-04-651	Lherzolite	Hand sample	Huangshanxi	0.8	27	15	58	9.4	4.8	47.8	36.7	2.0	5.3	n.a.	n.a.	n.a.	/
06-04-672.6	Lherzolite	Hand sample	Huangshanxi	1.8	13	10	77	4.6	3.1	53.9	37.7	1.5	12.4	85.5	1146.0	96.3	7.8
06-04-711.5	Lherzolite	Hand sample	Huangshanxi	1.4	15	14	70	5.4	4.5	51.9	37.4	1.2	10.1	85.8	921.0	118.7	11.7
06-18-944.3	Lherzolite	Hand sample	Huangshanxi	1.7	15	9	76	5.2	2.9	53.4	37.6	1.8	10.9	81.9**	632.0**	222.0**	20.4
06-18-919	Lherzolite	Thin section	Huangshanxi	4.0	20	11	69	7.0	3.6	51.2	37.2	2.0	7.6	n.a.	n.a.	n.a.	/
06-04-626.7	Lherzolite	Thin section	Huangshanxi	2.5	18	9	73	6.2	2.8	52.6	37.4	2.2	8.9	85.9	1088.0	101.7	11.4
06-04-651	Lherzolite	Thin section	Huangshanxi	1.8	26	21	53	9.3	6.5	46.7	36.6	1.4	5.3	n.a.	n.a.	n.a.	/
06-04-672.6	Lherzolite	Thin section	Huangshanxi	3.1	19	9	72	6.7	2.8	52.3	37.5	2.4	8.2	85.5	1146.0	96.3	11.7
06-04-711.5	Lherzolite	Thin section	Huangshanxi	1.5	13	23	63	4.7	7.4	50.0	37.3	0.6	11.2	85.8	921.0	118.7	10.6
06-18-944.3	Lherzolite	Thin section	Huangshanxi	1.4	15	21	64	5.2	6.7	50.1	37.2	0.8	10.2	81.9**	632.0**	222.0**	21.8
ZK3693-279	Pl ol websterite	Thin section	Xiangshanzhong	1.9	14	28	58	4.6	9.0	48.8	37.1	0.5	11.1	80.2	978.2	150.1	13.5
ZK3693-296	Pl ol websterite	Thin section	Xiangshanzhong	2.3	16	18	66	5.5	5.7	50.9	37.3	1.0	9.7	81.4	1100.0	122.2	12.6
ZK3693-308	Pl ol websterite	Thin section	Xiangshanzhong	3.0	13	12	75	4.6	3.7	53.5	37.8	1.2	12.3	79.0	1249.3	170.0	13.8
ZK3693-341	Pl ol websterite	Thin section	Xiangshanzhong	2.2	11	7	81	3.8	2.2	55.5	37.9	1.7	15.5	78.0	978.2	195.0	12.6
HSN455	Pl lherzolite	Hand sample	Huangshannan	6.6	41	8	51	###	2.4	45.9	36.0	6.0	3.4	n.a.	n.a.	n.a.	/
14HSN36	Ol websterite	Hand sample	Huangshannan	6.1	38	6	56	###	1.8	47.4	36.3	7.3	3.8	n.a.	n.a.	n.a.	/
15-4-7	Pl lherzolite	Thin section	Huangshannan	4.7	45	22	33	###	6.9	40.4	35.2	2.3	2.7	n.a.	n.a.	n.a.	/
TD545-4	Gabbro	Thin section	Tudun	13.6	15	2	83	5.5	0.5	55.5	38.0	10.9	10.5	n.a.	n.a.	n.a.	/
TD505-2	Gabbro	Thin section	Tudun	13.7	10	7	83	3.6	2.3	55.6	38.1	1.6	16.2	n.a.	n.a.	n.a.	/
TD545-1	Gabbro	Thin section	Tudun	8.7	13	9	78	4.9	2.7	54.1	37.8	1.8	11.6	n.a.	n.a.	n.a.	/
ZK11-1-197.5	Pl lherzolite	Thin section	Tudun	1.8	18	21	61	6.8	6.6	48.8	37.0	1.0	7.5	83.0	1239.2	90.0	12.0
ZK11-179.5	Pl lherzolite	Thin section	Tudun	3.0	15	18	67	5.5	5.6	51.0	37.3	1.0	9.8	83.1	1382.8	86.2	8.8
ZK11-1-201	Pl lherzolite	Thin section	Tudun	3.3	14	35	51	5.3	11.3	46.1	36.7	0.5	9.2	83.2	1183.8	106.0	11.5
ZK11-1-206.5	Pl lherzolite	Thin section	Tudun	2.1	13	14	73	4.9	4.4	52.5	37.6	1.1	11.3	83.0	1030.2	123.8	10.9
22-2-838	Wehrlite	hand sample	Poyi	1.4	47	13	40	###	4.1	45.9	35.3	3.2	3.7	n.a.	n.a.	n.a.	/
22-4-867	Wehrlite	hand sample	Poyi	1.7	58	19	22	###	6.0	41.5	34.3	2.7	2.7	n.a.	n.a.	n.a.	/
PYZK23-3-761	Wehrlite	Thin section	Poyi	1.3	56	33	11	###	10.4	37.8	34.4	1.5	2.5	90.0**	2514.5*	31.8**	12.8
PYZK23-3-1057	Wehrlite	Thin section	Poyi	1.8	44	20	36	###	6.2	42.4	35.3	2.3	3.2	90.2**	3300.3*	24.0**	7.5
PYZK23-3-948	Wehrlite	Thin section	Poyi	0.7	44	17	38	###	5.4	43.3	35.3	2.7	3.1	90.5**	2357.3*	32.2**	10.3
S*-sulfur content calculated based on the volume proportion of the XRF image of S, Pn-pentlandite, Cpy-chalcopyrite, Po-pyrrhotite																	
n.a.-not analyzed; 81.9**-data from Mao et al., 2014 and Xue et al., 2016																	
/-value has not been calculated due to significant sulfide fractionation or to absent of data																	

1114

1115

1116

1117

1118

1119

1120

1121 Table 5. Summary of the average compositions of olivine and sulfide for the Ni–Cu

1122 deposits in NW China.

Deposit	Location	Host rock	Olivine composition						Sulfide composition								Data source
			Fo	$\sigma$	Ni	$\sigma$	Fe/Ni	$\sigma$	Ni	$\sigma$	Cu	$\sigma$	Cu/Ni	$\sigma$	Fe/Ni	$\sigma$	
			mol. %	mol.%	ppm	ppm			wt.%	wt. %	wt.%	wt.%					
Kalatongke	East Junggar	Ol gabbro	76.5	2.2	1327	295	137.4	11.9	3.4	1.4	6.1*	3.0	1.8	1.1	19.2	9.8	This study, Li et al., 2012; Gao et al., 2012; Zhang et al., 2009
Huangshandong	North Tianshan	Lherzolite, Ol websterite	82.5	2.0	1269	194	101.7	16.6	6.1	0.9	2.2	1.1	0.4	0.2	9.1	1.3	Mao et al., 2015; Sun et al., 2013b
Huangshandong	North Tianshan	Ol gabbro	73.0	3.0					5.2	2.6					10.4	6.9	Mao et al., 2015; Sun et al., 2013b
Huangshanxi	North Tianshan	Lherzolite	83.5	1.2	1094	260	118.7	25.5	6.8	1.8	2.9	2.6	0.4	0.4	7.4	2.2	This study; Mao et al., 2014a; Zhang et al., 2011
Huangshannan	North Tianshan	Lherzolite, Ol websterite	85.9	1.0	2714	163	37.6	9.8	###	1.1	2.2	1.0	0.1	0.1	2.8	0.30	Mao et al., 2016; Zhao et al., 2016
Xiangshanzhong	North Tianshan	Pl lherzolite, Pl ol websterite	79.5	2.6	1084	162	149.2	26.5	4.6	0.6	5.2*	2.5	1.1	0.6	11.7	1.2	This study; Tang et al., 2013
Tudun	North Tianshan	Lherzolite, Pl lherzolite	83.0	0.7	1379	71	101.3	11.6	5.6	0.7	3.2	1.1	0.6	0.1	7.5	1.9	This study
Tulaergen	North Tianshan	Pl lherzolite	82.4	2.8	1189	251	107.0	18.7	8.8	2.5	3.8	1.5	0.4	0.2	5.7	1.9	Sun, 2009
Hulu	North Tianshan	Lherzolite	83.4	2.3	786	192	167.1	55.5	5.0	1.8	2.5	1.4	0.5	0.3	10.9	3.1	Sun, 2009; Zhao et al., 2016
Tianyu	Central Tianshan	Lherzolite	80.4	0.8	677	83	223.6	35.4	4.0	1.5	4.5	4.4	1.1	1.0	13.6	3.2	Tang et al., 2011
Poyi	Beishan	Dunite, Wehrlite	88.0	1.2	2318	601	30.0	2.4	###	0.6	5.5	2.2	0.4	0.2	3.0	0.2	This study; Xue et al., 2016
Fo=100×Mg/(Mg+Fe), $\sigma$ -Standard deviation.																	
Sample with sulfur content >1 wt.% is used for 100% sulfide calculation, samples that have experienced sulfide fractionation and percolation were not included.																	
Cu tenors in sulfides was estimated from whole rock Ni, Cu, S contents, where these label with * were calculated from XRF images.																	

1123

1124

1125

1126

1127

1128

1129

1130

1131 Table 6. Coefficients and uncertainty of equation (3) for regression of experimental

1132 measurement of  $K_D$ .

1133

$K_D = a + b \cdot C_{Ni} + c \cdot \Delta QFM$		
	Coefficient value	$\sigma$
a	9.775	1.105
b	0.416	0.033
c	-4.308	0.440

1134

1135

1136

1137 Table 7. Modeling results of olivine composition and Ni tenor in sulfides during the

1138 fractionation of the parental magma and parameters used in modeling.

	Fractionation								Contamination		
Crystallized phase		Ol	Ol	Ol	Ol	Ol	Ol+Cpx+Pl*	Ol+Cpx+Pl*			
F (%)	100	95	90	85	78	74	78	74	10**	20	Avg Crust*
<i>Magma composition</i>											
MgO (wt.%)	14.91	13.04	11.12	9.05	5.86	3.99	5.86	3.99	13.89	12.86	4.66
FeO (wt.%)	9.31	9.28	9.18	8.98	8.38	7.74	8.38	7.74	8.98	8.66	6.04
Ni in magma (ppm)	583	444	327	203	71	25	134	79	536	496	59
<i>Olivine composition</i>											
Fo in olivine (mol.%)	90.0	89.3	87.8	85.7	80.0	75.0	80.0	75.0	90.2	89.9	
Ni in olivine (ppm)	3500	2934	2287	1826	918	420	918	420	3214	3273	
<i>Ni tenor at different R values(wt.%)</i>											
500	13.3	10.9	8.4	5.6	2.0	0.7	3.8	2.3			
1000	17.2	14.4	11.3	7.7	2.7	1.0	5.2	3.3			
2000	20.2	17.1	13.7	9.5	3.4	1.3	6.5	4.2			
7000		19.8	16.0								
$D_{Ni}^{olivine-silicate}$	6.0	6.6	7.0	9.0	13.0	17.0	13.0	17.0			
$D_{Ni}^{sulfide-silicate}$	419	477	529	615	637	729	637	729			
F-fraction of residual liquid after fractionation, Ol+Cpx+Pl*-Olivine, clinopyroxene, and plagioclase fractionation after F=85											
Avg Crust*-FeO and MgO concentrations of the average crust are from Rudnick and Gao (2003). **-. percentage of crustal contamination											
$D_{Ni}^{olivine-sulfide}$ is calculated from the host magma compositions from the previous studies of the Huangshandong, Huangshanxi deposits, using the equation of Li and Ripley (2010)											
$D_{Ni}^{sulfide-silicate}$ is calculated based on the equation of Kiseeva and Wood (2013): $\log D_{Ni} = 3.83 - 0.84 \cdot \log FeO$ , whereas FeO equals $FeO_{magma} / [Fe/(Fe+Ni+Cu)]_{sulfide}$											

1139